Materials Science and Engineering R 70 (2010) 303–319

Contents lists available at ScienceDirect

Materials Science and Engineering R

journal homepage: www.elsevier.com/locate/mser

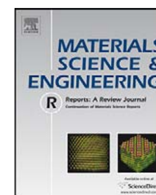

In situ TEM investigation of dynamical changes of nanostructures

L.J. Chen [a,*], W.W. Wu [b]

[a] Department of Materials Science and Engineering, National Tsing Hua University, Hsinchu 300, Taiwan, ROC
[b] Department of Materials Science and Engineering, National Chiao Tung University, Hsinchu 300, Taiwan, ROC

ARTICLE INFO

Article history:
Available online 2 July 2010

Keywords:
In situ TEM
Dynamical changes
Nanostructures
Epitaxial growth
Si nanorings
Si bicrystals
Silicide nanowires
Cu electromigration
Nanothermometry

ABSTRACT

In situ investigation of the temperature induced phase transformation, structural and chemical evolution of nanocrystals is important for understanding the structure and stability of nanomaterials. Transmission electron microscopy (TEM), one of the most powerful tools for characterizing nanostructured materials, is essential for the development of nanotechnology. In situ TEM is a technique that allows a direct observation of dynamic properties in nanoscale. Recent development of ultra-high vacuum TEM (UHV-TEM) further enables the investigation on atomic-scale materials systems in a clean environment. The appropriate utilization of the UHV-TEM will be beneficial in studying the fundamental mechanisms of dynamic reactions, formation of transient phase, solid-state amorphization, epitaxial growth, growth kinetics and evolution of defects. In this paper, we present the most recent progress in observing dynamic processes in nanoscale by in situ UHV-TEM.

© 2010 Elsevier B.V. All rights reserved.

Contents

1. Introduction . . . 303
 1.1. In situ electron microscopy and nanotechnology . . . 303
2. Growth of nanostructures on Si . . . 304
 2.1. Formation and evolution of self-assembled crystalline Si nanorings on (0 0 1)Si mediated by Au nanodots [9] . . . 304
 2.2. Collective movement of Au nanoparticles on a silicon bicrystal [19] . . . 306
 2.3. Directed movement of Au–Si droplets towards buried dislocation network on silicon bicrystals [33] . . . 308
 2.4. Growth of high-density titanium silicide nanowires in a single direction on a silicon surface [37] . . . 309
3. Nano-silicide formation from Si nanowires . . . 310
 3.1. Controlled growth of atomic-scale Si layer with huge strain in the nano-heterostructure NiSi/Si/NiSi through point contact reaction between nano-wires of Si and Ni and reactive epitaxial growth [47,48] . . . 310
 3.2. Repeating events of nucleation in epitaxial growth of nano-$CoSi_2$ and NiSi in nanowires of Si [58,59] . . . 312
4. In situ TEM investigation of copper electromigration . . . 314
 4.1. In situ transmission electron microscope observations of electromigration in copper lines at room temperature [64,65] . . . 314
 4.2. Observation of atomic diffusion at twin-modified grain boundaries in copper [77] . . . 316
5. Growth kinetics of semiconducting nanowires [3,80] . . . 317
6. Nanothermometry . . . 317
7. Conclusions . . . 318
 Acknowledgements . . . 318
 References . . . 318

1. Introduction

1.1. In situ electron microscopy and nanotechnology

Low-dimensional nanostructures, such as nanodots, nanowires and nanotubes, are essential building blocks for developing a bottom-up approach for nanotechnology-enabled architectures. Zero-dimensional nanocrystals have been a subject of intense study.

* Corresponding author.
E-mail address: ljchen@mx.nthu.edu.tw (L.J. Chen).

0927-796X/$ – see front matter © 2010 Elsevier B.V. All rights reserved.
doi:10.1016/j.mser.2010.06.014

The nanodots exhibit unique physical properties owing to the small size and quantum effects. The dynamical change of nanodots during growth is not only of interest itself; it may also provide key understanding for the thin film growth. On the other hand, metallic nanowires and nanotubes can both act as interconnects for the transport of charge carriers as well as active device elements. Semiconductor nanowires offer all the properties of traditional semiconductors, such as excellent control of the electrical and optical properties, as well as new benefits including possible carrier mobility enhancements for less scattering attributed to reduction in dimension. A wide variety of nanowires can be synthesized from group IV, III–V, and II–VI materials, and can be exploited to make a myriad of nanoscale devices, from transistors to light emitting diodes and biosensors. These developments suggest that nanowires are excellent candidates for bottom-up assembly of architecturally complex integrated devices system [1–6].

As the critical dimensions for devices become smaller, it is necessary to precisely specify the crystal structures, interface morphology, shapes and sizes of individual features; also, control in atomic scale is essential. Achieving this level of control requires a detailed understanding of fundamental processes which occur during processing. State-of-the-art atomic-resolution instruments and techniques, such as UHV-TEM, variable temperature scanning tunneling microscope (VT-STM) and atomic resolution TEM, are utilized to investigate the structures and dynamic changes in several technologically important materials systems, such as Si-based nanowires and semiconducting oxide nanostructured materials. Through observation of mass transport, phase transition and/or growth in situ, one can understand the basic mechanisms and model relevant processes [7,8].

This review covers the recent advances in the investigations of dynamic changes of nanostructures utilizing in situ UHV-TEM. The examples include: (1) growth of nanostructures on Si, (2) nano-silicide formation from Si nanowires, (3) in situ TEM investigation of copper electromigration and (4) growth kinetics of semiconducting nanowires.

The electron beam voltage and emission current were set to be 200 KeV and 5 μA, respectively. All the TEM images were taken from "top-view". For the preparation of samples, the samples in examples (1) and (3) are Si substrate prepared by chemical etching. During the in situ observation, the heating of example (1) was by directly applying current through Si. For example (2), metal and Si nanowires were dispersed on Cu grids covered with SiO_2. The heating was realized by applying current to the filaments of the special holder.

2. Growth of nanostructures on Si

2.1. Formation and evolution of self-assembled crystalline Si nanorings on (0 0 1)Si mediated by Au nanodots [9]

Nanorings, which are artificial nanoscale clusters that confine electrons in three dimensions, are attractive due to their unique physical properties of large and negative excitonic permanent dipole moment [10], high oscillator strength for the ground-state band-to-band transition [11], possible tunable electronic states [12], and optical emission from a charged single nanoring [13]. Nanorings of various materials have been fabricated, especially for III–V compound semiconductors based on the growth of thermodynamic [14] and kinetic models [15]. However, the investigations on Si-based nanorings have been scarce [16,17].

Single-crystal, 3–5 Ω cm, phosphorous-doped (0 0 1) Si wafers were used in the present study. Si wafers were cleaned chemically by a standard Radio Corporation of America (RCA) cleaning process. A 2-nm-thick Au thin film was then deposited onto Si substrates at room temperature in an electron-beam evaporation system. The vacuum was better than 5×10^{-6} Torr during the deposition of ultrathin Au films. For the formation of Au nanodots, rapid thermal annealing (RTA) was employed in a high-purity N_2 atmosphere at 400 °C for 30 s. Finally, the samples were placed into a tube furnace. After the tube had been evacuated for several hours to remove O_2 from the system by a rotary pump to a pressure of 1×10^{-3} Torr, the samples were heated to 1050 °C at a rate of 5 °C/min and held at 1050 °C from 5 s to 2 h in an ambient with Ar + 5% H_2 flowing through the tube.

The growth of high-density Si nanorings has been achieved on ultrathin Au films on silicon substrate. Au nanodots, 12 nm in average size, were formed on Si substrate in the samples annealed at 400 °C for 30 s. After annealing at 1050 °C, surface morphologies were observed to change drastically. A typical atomic force microscope (AFM) image reveals that the formation of a high density of ring-shaped nanostructures in a sample after annealing at 1050 °C for 2 h, as shown in Fig. 1(a). Energy dispersive X-ray

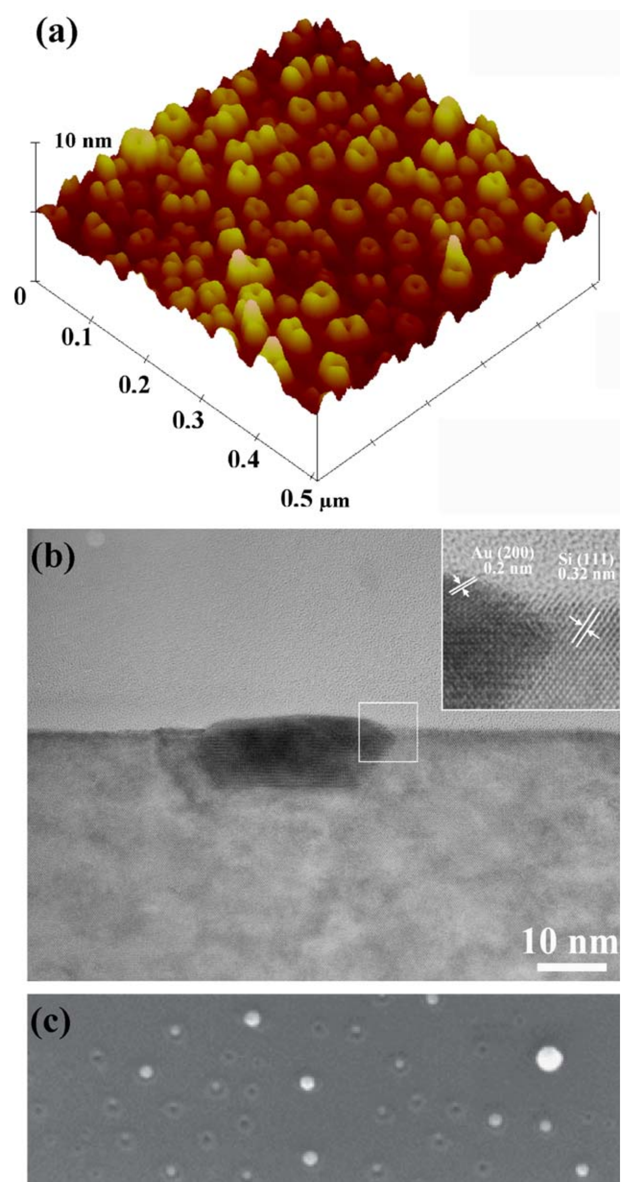

Fig. 1. (a) AFM image showing the formation of Si nanorings in a sample annealed at 1050 °C for 2 h, (b) high resolution TEM (HRTEM) image showing the recess of an Au nanodot at centers of nanorings in a sample annealed at 1050 °C for a few seconds. Inset is the high magnification image of the outlined region, (c) SEM image shows the morphology of Si nanorings [9].

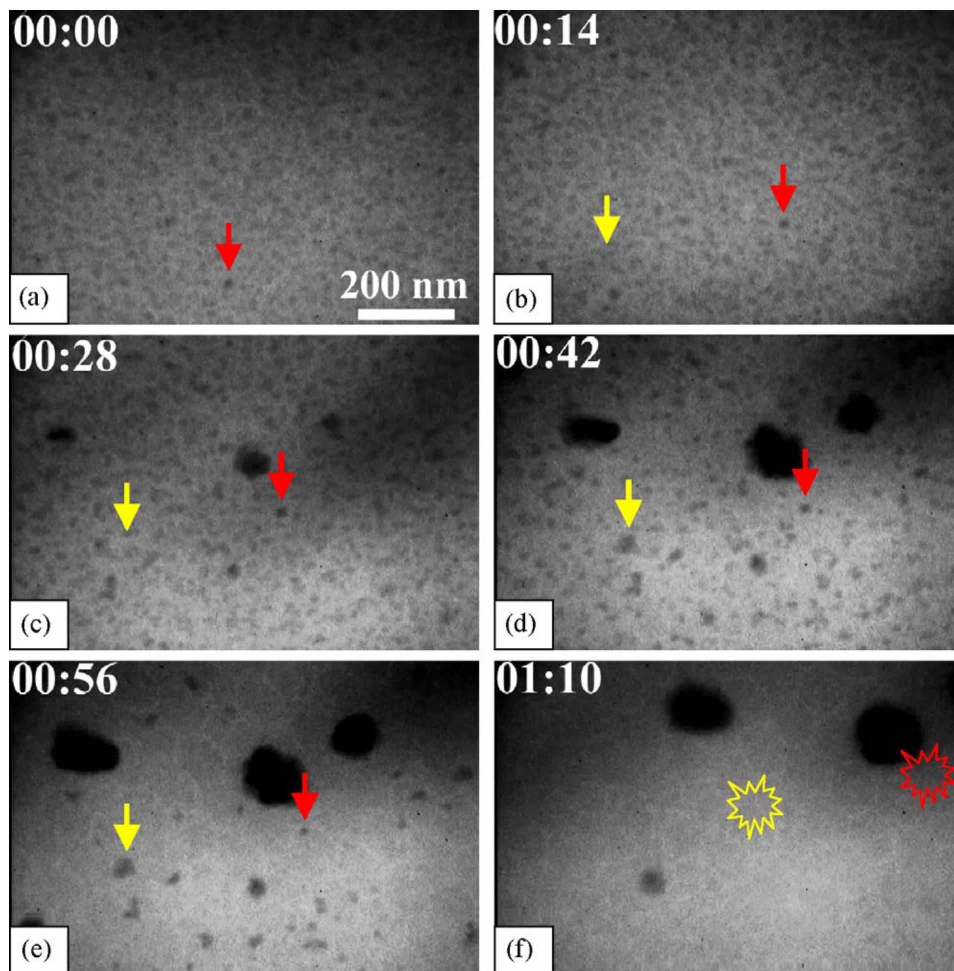

Fig. 2. A sequence of in situ UHV-TEM images of Au–Si nanodots with different annealing times as indicated in minutes and seconds at 1050 °C [9].

spectroscopy (EDS) measurements revealed that the surface is free from Au. The disappearance of the Au atoms will be discussed in a later paragraph. The density of nanorings was determined to be about $4.3 \times 10^{10}\,\mathrm{cm}^{-2}$. In addition, nanorings have a narrow distribution of height and diameter of 1.4 ± 0.3 and 24.9 ± 4.0 nm, respectively. Fig. 2 shows the burrowing of Au nanodot into the silicon substrate. The Au nanodot was observed to be surrounded by the Si nanoring, as seen in the inset of Fig. 1(b). The atomic image reveals that Si nanoring is grown epitaxially on (0 0 1)Si. The presence of shrunk Au nanodots at the centers of nanorings corroborates the suggestion that the formation of nanorings is mediated by Au nanodots. Fig. 1(c) shows SEM image of Si nanorings.

The evolution of the formation of nanorings was elucidated by in situ UHV-TEM observations. Images captured from the video were acquired for the same region so that the dynamic development of nanorings from Au–Si eutectic droplets was observed, as shown in Fig. 2. The liquid Au–Si alloy droplets are expected to form on the surface of Si substrate at a temperature above the eutectic temperature of the Au–Si (363 °C). After the sample was flashed at 1000 °C for cleaning in a pretreatment chamber, the Au islands were formed, as shown in Fig. 2(a). The Au–Si liquid droplets underwent the growth-coarsening process as well as change in shape during the observation, as seen in Fig. 2(b)–(f), indicating a change in surface tension resulted from the variation in composition. It has been reported that with SiO_2 on the surface, some Au will aggregate through surface diffusion [3]. We also observed this phenomenon. In addition, Au was identified from cross-sectional HR TEM images. Lower density of droplets was observed after prolonged annealing. It is remarkable that most of the Au–Si droplets remained and did not migrate away after prolonged annealing at such a high temperature. On the other hand, most Au–Si droplets faded away suddenly instead of coalescing with one of their neighbors in 2 min at 1050 °C under UHV. The disappearance of Au nanodots was rather abrupt. It suggested that the diffusion of Au atoms into Si should not be the dominant cause of disappearance of Au nanodots. Owing to the lack of experimental data on vapor pressure of Au–Si eutectic alloy at 1050 °C (near Au melting point: 1063 °C), the vapor pressure of Au–Si eutectic alloy is deduced from the vapor pressures of the Au and Si by linear interpolation herein. Clausius–Clapeyron equation, applicable to both liquid/gas or solid/gas equilibrium curves, is used to determine to vapor pressure with annealing temperature [18]:

$$\ln\frac{P_2}{P_1} = \frac{-\Delta H_{\mathrm{vap}}}{R}\left(\frac{1}{T_2} - \frac{1}{T_1}\right) \quad (1)$$

where ΔH_{vap} is the enthalpy of vaporization (J/mol), R is the gas constant and equal to 8.3145 J/mol K, T is the temperature in K, and P is the vapor pressure in Torr. The enthalpies of vaporization at boiling points of Au and Si at 760 Torr of Au and Si are (330 kJ/mol and 2856 °C) and (359 kJ/mol and 2900 °C), respectively. Therefore, the vapor pressures of Au and Si are calculated to be 2.3×10^{-5} Torr and 4.1×10^{-6} Torr at 1050 °C, respectively. It can be inferred that the evaporation of Au–Si alloy is severe inside the UHV chamber with a pressure of 3×10^{-10} Torr at 1050 °C during the in situ investigation. As a result, it is concluded that the Au nanoparticles evaporated and left behind a nanoring structure at 1050 °C.

2.2. Collective movement of Au nanoparticles on a silicon bicrystal [19]

Understanding the growth and behavior of metal clusters on a specific substrate is of prime importance in a wide range of areas. Indeed such clusters may be used as the active parts in catalysts [20,21]. Cluster growth has been the subject of intensive research for decades. There have also some studies which allow one to deduce the mechanisms in nucleation and coalescence regimes [22–27].

Silicon bicrystal has been the potential substrate for nano-devices due to its highly regular and controllable surface variation. The image force, induced by the buried dislocation, leads to the variation in strain field at the surface [28]. Au nanoparticles have been shown to be an excellent catalyst for the growth of many important nanostructures [4,5,14,15,29].

The silicon bicrystal was fabricated by hydrophobic bonding a (0 0 1) silicon wafer to a silicon-on-insulator (0 0 1) wafer with 30-nm-thick top silicon layer (Si (30 nm)/SiO_2 (145 nm)/Si(0 0 1)). The thickness of the remaining top Si layer can be accurately controlled to be as thin as 20 nm by the sacrificial thermal oxidation at 900 °C. 1-nm-thick Au thin film was deposited on the silicon bicrystal substrate by electron beam evaporation at room temperature. The sample was then transferred into the UHV-TEM without breaking the vacuum. TEM examinations were carried out at 250 °C.

A series of electron micrographs showing the gradual change of Au clusters in the same area are shown in Fig. 3. The images were selected from a video file recorded over a period of about 45 s. The dislocation grid has a spacing of 7 nm for a bicrystal misorientation of 3.14°. The Au clusters are semi-spherical in shape, as those on blank Si substrate, but confined by the dislocation grids on silicon bicrystal. Upon annealing, Au atoms agglomerated to form clusters with sizes up to 3×3 grids, i.e. 21 nm in size (Fig. 3 (a)). A theoretical model was proposed for self-assembly of 3D metal islands, indicating the islands are influenced by edge and/or strain effects. Furthermore, the edge effect induces a stable island size against coarsening [30]. Au clusters were found to be confined by the dislocation grids, highlighting both strain and edge effects, on the silicon bicrystal surface.

Fig. 3(a)–(c) shows the change of small clusters. With reference to video file, it appears that the disappearance of cluster led to the protrusion of cluster 4 at the side facing cluster 1 (Fig. 3(a) and (b)). Using the other clusters nearby as reference marks, it can be seen that clusters 2 and 3 move to the right and downward, respectively, by a distance of one dislocation grid spacing (Fig. 3(b) and (c)). The continuing morphological change with transient migrations of the Au clusters was evident. The "transient" is herein referred to the extreme short time duration of an independent migration in two or three continuous frames of the video images (i.e. ~within 1/10 s). In Fig. 3(d)–(f), clusters 5 and 6 exhibit the typical Oswald ripening behavior to the larger clusters in the vicinity. Cluster 5 shrank gradually until ultimate disappearance (Fig. 3(f)). On the other hand, the contrast of cluster 6 became weaker indicating that it was in the process of dissolution. The confinement of Au clusters by dislocation grids is apparent throughout the shrinkage process. The observation indicates that the stress field induced by the dislocation grid lines exerted strong influence on the shape and discontinuous change of Au nanoparticles. During the same period, cluster 4 grew substantially. The transient protrusion of both upper and lower edges (Fig. 3(e)) represents the initial stage of

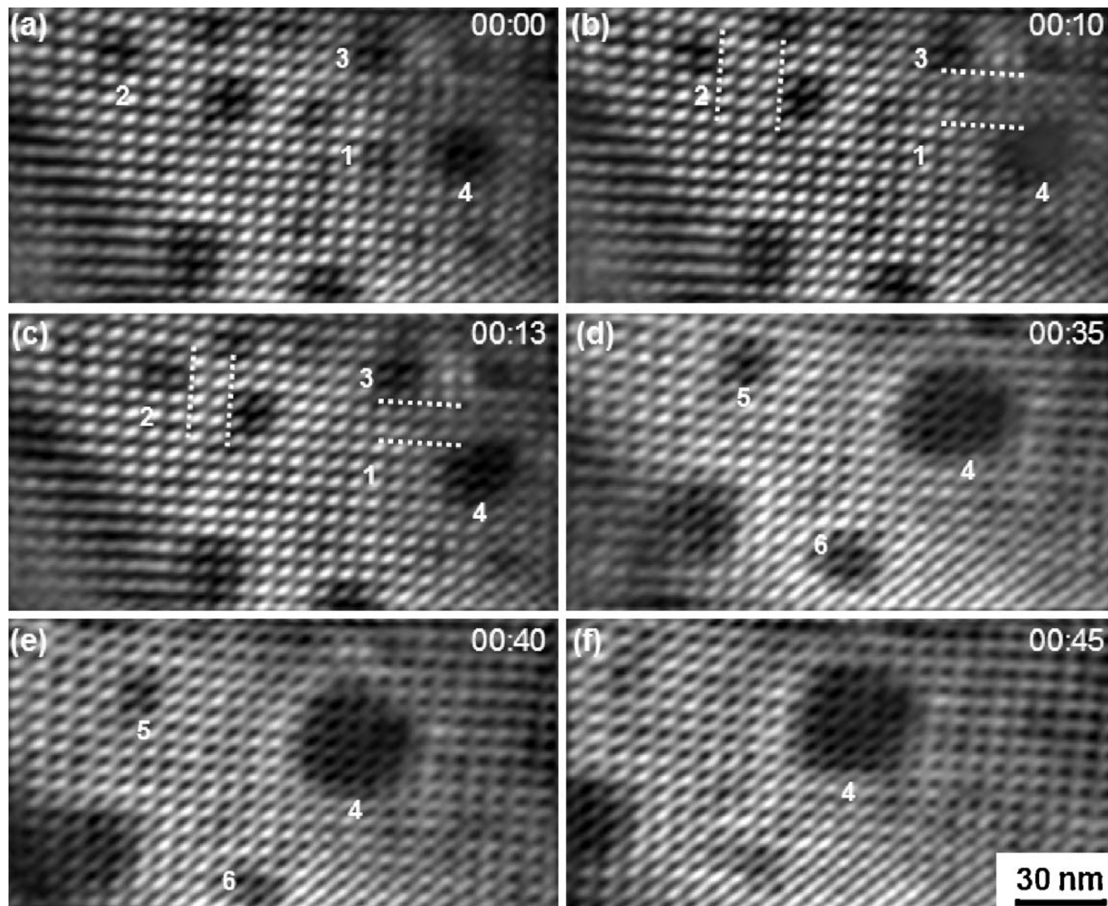

Fig. 3. Sequential images captured with real-time video illustrating collective mass transport of Au clusters on (0 0 1) silicon bicrystal at 250 °C. The clocking times are (a) 0 s, (b) 10 s, (c) 13 s, (d) 35 s, (e) 40 s and (f) 45 s [19].

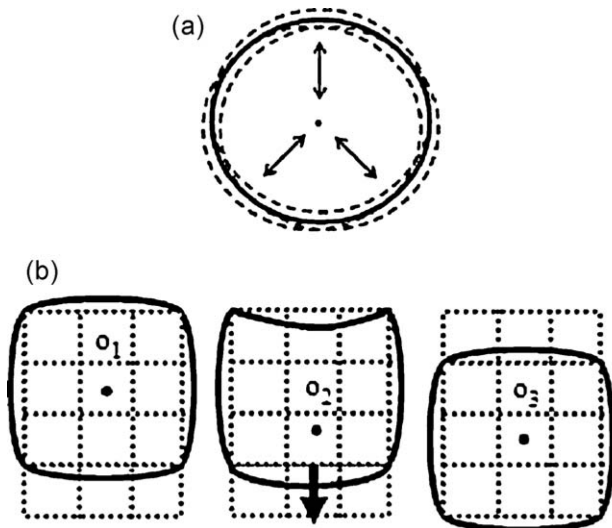

Fig. 4. Schematic plots of the movements of clusters on (a) blank silicon surface and (b) silicon bicrystal surfaces [19].

coarsening with atoms dissolved from the neighboring clusters smaller than the critical size. However, it soon morphed to conform to the dislocation grids (Fig. 3(f)).

Iijima and Ichihashi [31] investigated dynamic behavior of Au nanoparticles and observed abrupt change of its shape through internal transformation involving twins which took place in less than 0.1 s. This behavior also led to the shift of the center of gravity in any random direction. The Au island at this temperature was like a quasi-liquid crystal and viscous flow became the most possible mechanism of migration. The distribution of regular dislocation lines at the silicon bicrystal interface provided a means to visualize the movement of Au nanoparticles in real time. Fig. 4(a) and (b) shows schematic plots of movements of Au clusters on blank silicon and silicon bicrystal substrates, respectively.

The movement of the mass center of nanoparticles under thermal agitation has often been considered as the "Brownian motion", which means that clusters can move in any directions without any constraint. For Au clusters moved on a blank Si surface, the transient collective movement similar to that on the

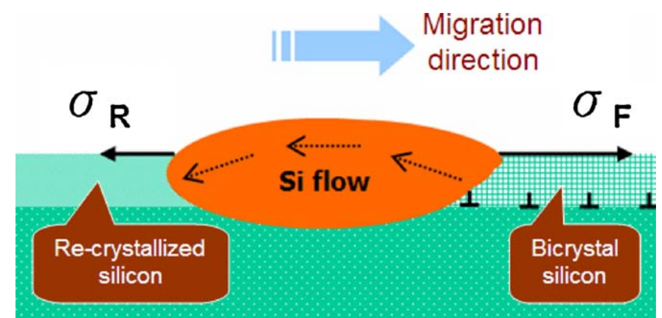

Fig. 6. A schematic model for the evolution of Au–Si droplet on Si bicrystal. The arrows with dotted lines indicate the Si flow diffusion into and through the droplet. The arrows with full lines indicate the unbalanced surface [33].

silicon bicrystal was never observed. It is conjectured that for the clusters on blank Si substrate, the shape accommodation is relatively easy without constraint to adjust its mass movement (Fig. 4(a)). As a result, the typical Oswald ripening with accompanying dissolution and coarsening was observed. On a silicon bicrystal surface, Oswald ripening is still significant. However, viscous flow transport became evident with the presence of grid lines. As seen in Fig. 4(b), the Au island was originally confined by the dislocation grids. If the mass of Au island re-condenses at one side, its contact angle will change and induce the re-entrant angle to allow internal transformation by twinning immediately. Within a very short time (<1/30 s), the cluster migrated along particular direction and was then confined by the next grid. The motion of the cluster was no longer "Brownian." Furthermore, the shapes of confined islands were defined by the strain field modulated by the presence of buried screw dislocation grids in the silicon bicrystal. The influence appears to be more significant than that specified by a theory proposed by Bourett, which predicted that screw dislocations are two orders of magnitude less effectives than edge dislocations to affect the location of nanoparticles [32]. The present result shall serve as a good reference to refine the theory to realize the control of self-organized nanoparticles on silicon bicrystal. It is worth mentioning that at the scale of 20 nm or so, the melting temperature lowing of Au dots should be significant. However, in this experiment, the temperature is only 250 °C. Moreover, as the temperature

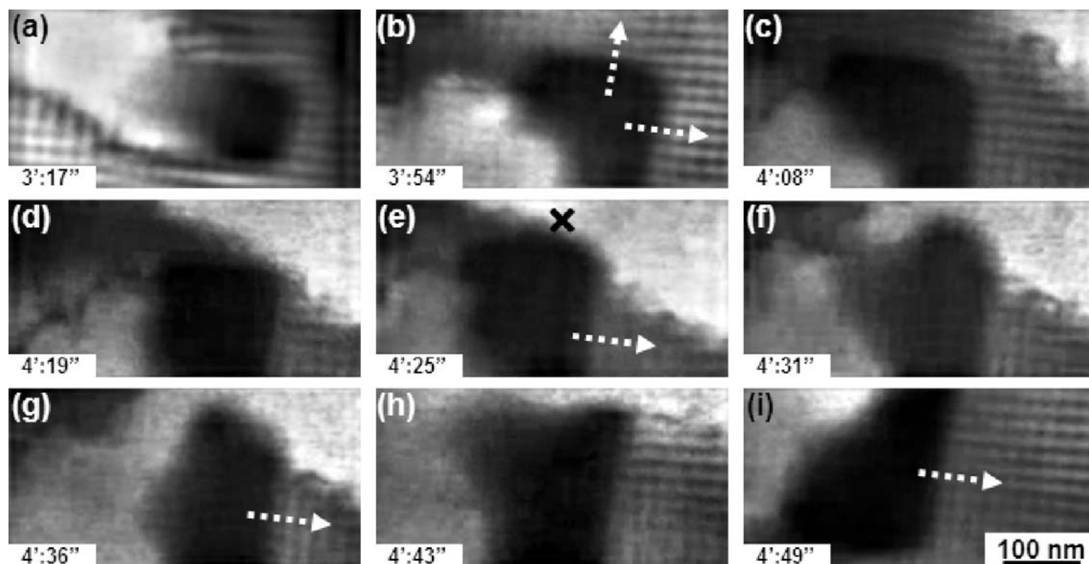

Fig. 5. Sequent in situ images of Au–Si droplet migration on Si bicrystal at 500 °C. It demonstrates that the moving front was confined by dislocation grids and the motion path was strictly guided by the existence of buried dislocation [33].

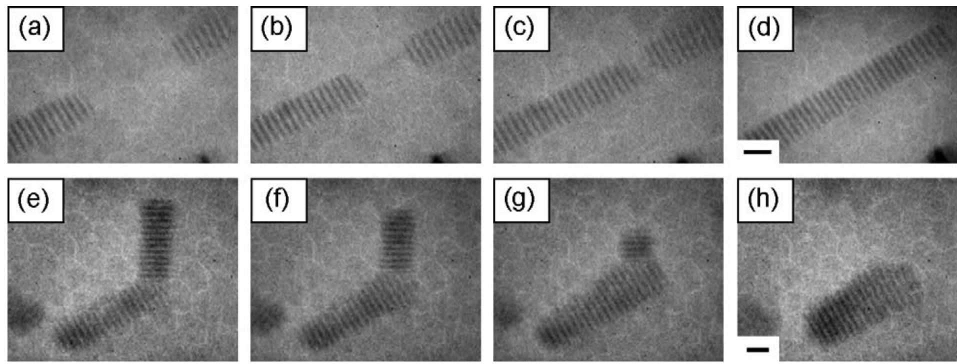

Fig. 7. In situ TEM images of the interactions of titanium silicide nanowires at 700 °C. The images of nanowires in the same direction were obtained at elapsed times of (a) 0 min, (b) 9 min, (c) 18 min, and (d) 19 min. The images of nanowires in different directions were obtained at elapsed times of (e) 0 s, (f) 25 s, (g) 49 s, and (h) 80 s. The scale bars correspond to 6 nm in (d) and 4 nm in (h) [37].

increases, the eutectic reaction between Au and Si occurs to form Au–Si droplets at a temperature far below the melting temperature of Au.

To clarify the effect of electron beam damage, experiments with electron beam on and no direct heating were conducted. No change was found to occur even after exposure to electron beam for prolonged time. On the other hand, once the sample was heated or applied current to, abrupt change occurred. The result of control experiment indicates that the effect of electron beam damage was minimal.

2.3. Directed movement of Au–Si droplets towards buried dislocation network on silicon bicrystals [33]

The movement of nano-size liquid droplets on the solid surface has received increasing attention for the potential applications in the emerging areas of microfluidics. The behavior of fluids at the microscale can differ from macroscopic behavior in that factors such as surface tension and energy dissipation may dominate the system. Au–Si system is a model system for studying liquid alloy droplets. Among the various binary systems, Au–Si is the simplest as one of eutectic alloys without the complications of the existence of any stable intermetallic phase. The surface structure and interface stability of liquid Au–Si droplets on Si shall affect the shape and movement of the droplets.

Fig. 5 shows a series of images of the movement of Au–Si droplet at 500 °C. It is evident that a distinct trace (in bright contrast) is left behind the migrating path with the removal of buried dislocations (Fig. 5(a)). From both bright-field images and diffraction patterns, the bright contrast trace was found to correspond to single crystal silicon. The Au–Si droplet was observed to keep the flat front and the irregular-rim rear until it reaches the trail of another Au–Si droplet. The moving front of the droplet was largely confined by dislocation grids (Fig. 5(b) and (c)). The growth fronts are always parallel to dislocation network lines along ⟨1 1 0⟩ directions and apt to move along the ⟨1 −1 0⟩ directions of the perpendicular set of dislocation lines. When the droplet moved and encountered the trail which had been swept over by another droplet, it would evade and turn to the region with buried dislocation networks, as depicted in Fig. 5(d)–(g). In other

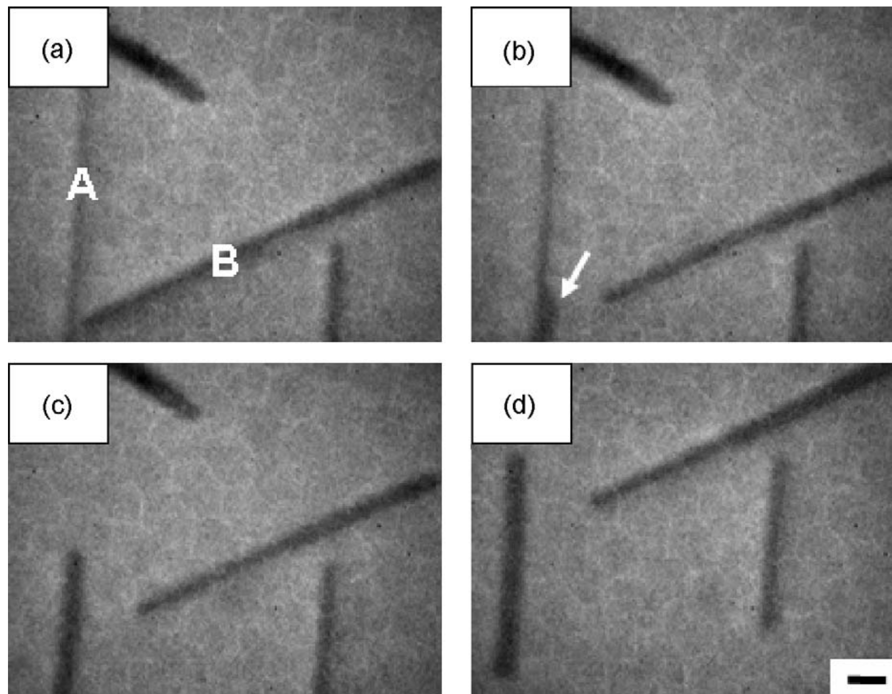

Fig. 8. In situ TEM images showing the interaction of one titanium silicide nanowire with another at its midsection at 700 °C. The images were obtained at elapsed times of (a) 0 s, (b) 16 s, (c) 56 s, and (d) 81 s. The scale bar corresponds to 30 nm [37].

words, the droplet tended to migrate only toward the region with buried dislocation networks. On the other hand, the movement of the flat fronts of the droplet was somewhat sluggish, i.e. the movement appeared to be retarded on the dislocation lines and slower than the parts neighboring the dislocation-free region. The region of droplet with gray contrast at the rear indicates that the droplet is thicker at the front than that at the rear indicating that the movement of the droplet was hindered by the presence of buried dislocations and the liquid droplet tends to accumulate near the flat front. The flat front had been maintained (Fig. 5(d)) before meeting the migrating trace of another droplet (Fig. 5(e) and (f)). The droplet was then steered to the region with dislocation grids (Fig. 5 (g)). As the front is lined up with dislocation grid, it started to move along the perpendicular direction again (Fig. 5(h) and (i)). Eventually, the droplet was quartered at a position without any surrounding undestroyed bicrystal area.

The formation and migration of eutectic metal-Si droplets were previously investigated. Yang et al. [34] concluded that the migration of Pt–Si eutectic droplet is due to the dissolution–diffusion–deposition flow of Si through the droplet driven by the Si concentration difference in the droplet following the temperature gradient. Bokhonov and Korchagin [35] found that the reaction flat front of eutectic Au–Si islands in Au/(0 0 1) Si is parallel to ⟨1 0 0⟩Si directions. In contrast, the moving flat fronts of Au–Si droplets on Si bicrystal are parallel to ⟨1 1 0⟩ directions of dislocation grids. The difference is resulted from the dominant influence of stress field of the buried dislocation network on the moving fronts of the droplets on the Si bicrystal. On the other hand, although the movement of Au–Si droplets on the Si bicrystal was not under a temperature gradient, it is possible that the mechanism of the migration of eutectic droplet via dissolution–diffusion–deposition flow of Si, concluded by Yang et al. may still be operating [34]. It is thought that the dissolution of buried dislocations lowered free energy of the system which drives the movement of eutectic alloy droplet. The precipitation of Si atoms from the supersaturated droplet formed a new strain-free single silicon layer, giving rise to an unbalanced solid surface tension at the different side of a droplet. This unbalanced tension due to the variation in surface structure leads to a driving force acting on the liquid without any temperature gradient. As a result, the migration of droplet under isothermal heating is driven by the stress generated by the buried dislocation network and is enhanced by the variation in solid surface structure. It is also consistent with the present in situ observation that the moving fronts of droplets are always ahead of the boundaries of eliminated dislocation network region. A schematic drawing of the process for the migration of Au–Si eutectic alloy droplets on silicon bi-crystal is illustrated in Fig. 6.

Wakayama et al. reported on the Au–Si alloy induced epitaxial growth of Si [36]. The growth behavior is similar to vapor–liquid–solid (VLS) growth [2], where Si precipitates at where Au is and then Au is pushed to the top end; also, there is epitaxial relationship between Au and Si interfaces. In the present in situ observation, Au–Si droplets tend to move toward the locations to eliminate surface defects and lower the total energy, the growth mechanisms are therefore very different.

2.4. Growth of high-density titanium silicide nanowires in a single direction on a silicon surface [37]

Nanowire-based materials have been synthesized for a wide range of materials such as metals, semiconductors and oxides [38–41]. Among these nanowires, a large number of epitaxial silicide nanowires have been investigated due to their low resistivity, small dimension and excellent compatibility with silicon device processing [42–45]. Semiconducting silicide nanowires can be used as active electric elements in integrated circuits. Metallic silicide nanowires have been studied as electrical interconnect and contact. The silicide nanowires exhibited novel physical and electrical properties as promising elements for future nanoscale devices. Understanding the formation mechanisms is a crucial step to the successful implementation of nanowires for practical employment. In situ UHV-TEM is an extremely valuable method for clarifying the growth mechanism of silicide nanowires since it can monitor in nanoscale the dynamic process as it occurs.

The interaction mechanisms of titanium silicide nanowires on Si(1 1 1) substrate were investigated by in situ UHV-TEM [37]. The $TiSi_2$ nanowires were oriented along three equivalent Si⟨1 −1 0⟩ directions and possessed small width and high aspect ratio. During continuous Ti deposition, the length of nanowires increased slowly, as visualized by the increase in the number of Moiré fringes, while the width did not change appreciably at the same time. When two nanowires grew in the same direction and eventually collided with each other, they would merge to form a single nanowire with the combined length of the two nanowires, as shown in Fig. 7(a)–(d). On the other hand, for two nanowires in different directions colliding with each other at the end, one of them collapsed to the other along the side of the nanowire and was absorbed by the other one, as shown in Fig. 7(e)–(h). The merging of the two nanowires in different directions occurred as a result of minimizing the total surface energy.

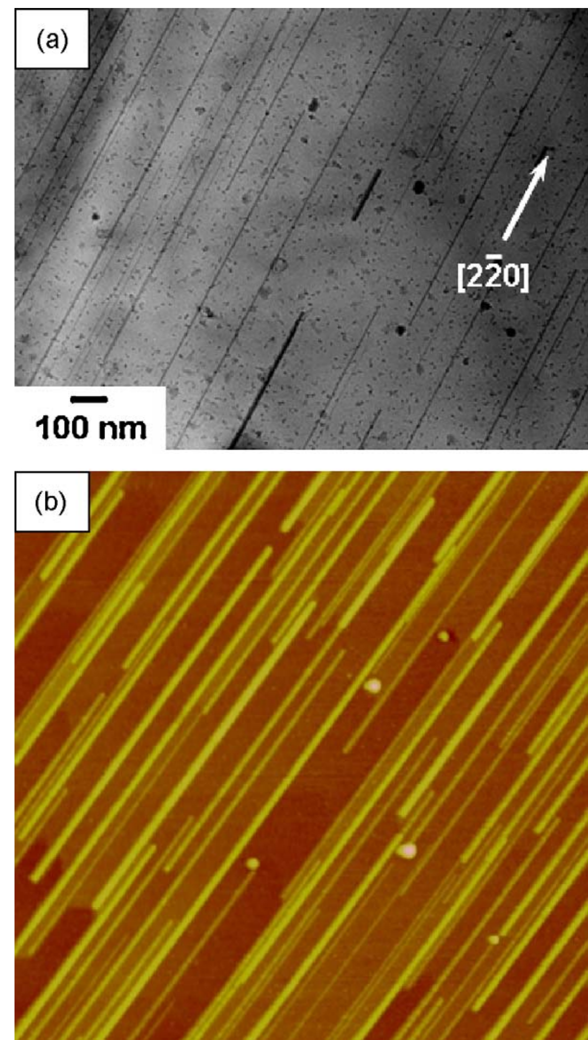

Fig. 9. Images of titanium silicide nanowires on Si(1 1 0). (a) TEM and (b) AFM (1.5 μm × 1.5 μm) images of titanium silicide nanowires grown on Si(1 1 0) along one [1–10] direction [37].

Fig. 8 shows as one $TiSi_2$ nanowire continued to grow and encounter the midsection of an inclined nanowire, it tended to recede rapidly and the other one became thicker at the midsection, as marked in Fig. 8(b) by the arrow. It indicates that the silicide atoms migrated from nanowires "B" to "A". According to the Gibbs–Thomson equation [46], the concentration is strongly related to the curvature along the nanowire ends. As a result, the concentrations of constituent atoms (Ti and Si) at the curved end of nanowire "B" are higher than those at the flat side of nanowire "A", resulting in the diffusion of Ti and Si atoms form nanowire "B" to "A". Owing to the supply of silicide for the nanowire "B" taking a relatively long time to arrive from the far end to the contact area, receding of the nanowire was observed.

Therefore, in order to grow a high density of long and high-aspect-ratio nanowires, it is highly desirable to grow nanowires along a single direction. This important insight has been fruitfully exploited to focus on the growth of titanium silicide nanowires on Si(1 1 0), since crystallographically the nanowires are favored to grow only in the [1–10] direction, as shown in Fig. 9. The results demonstrate the powerfulness of the in situ UHV-TEM observation. Most importantly, the achievement in controlled growth represents a significant advance in realizing the vast potential for applications of silicide nanowires in nanodevices.

3. Nano-silicide formation from Si nanowires

3.1. Controlled growth of atomic-scale Si layer with huge strain in the nano-heterostructure NiSi/Si/NiSi through point contact reaction between nano-wires of Si and Ni and reactive epitaxial growth [47,48]

As the end of the roadmap approaches for very-large-scale-integration of transistors on Si wafers, nanoscale transistor devices

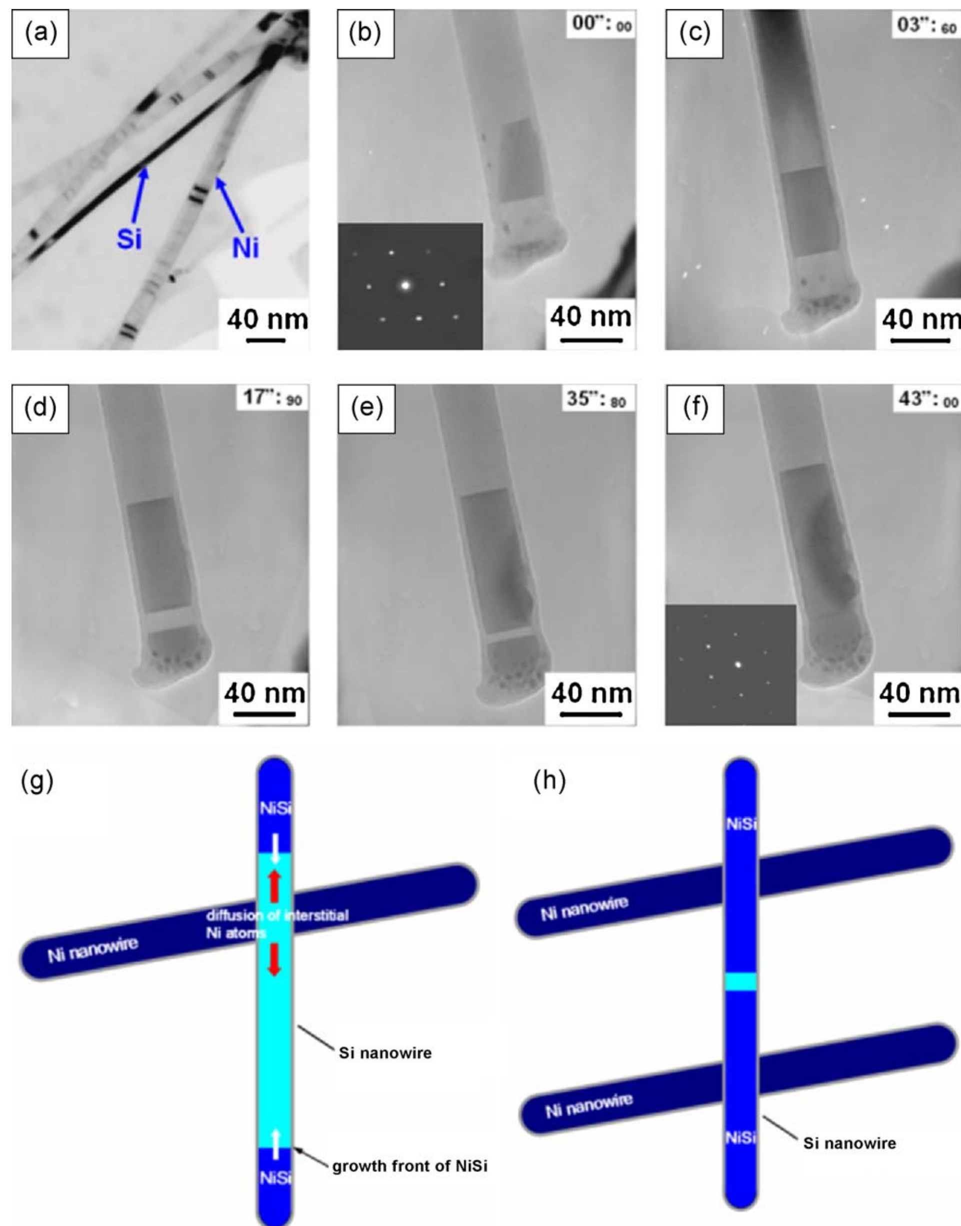

Fig. 10. Overview of NiSi formation within Si nanowires by point contact reaction. (a) A TEM image of Si and Ni nanowires dispersed on a Si_3N_4 membrane. (b–f) Sequence of in situ TEM images depicting the growth of a bamboo-type grain of NiSi within a Si nanowire at 700 °C. Inset in (b) selected area diffraction pattern showing the [1–10] zone axis of Si. Inset in (f) selected area diffraction pattern showing the [1–12] zone axis of NiSi. The time of the image capture is given in the rectangular box at the upper-right corner. The first two numbers are in unit of seconds and the following two smaller numbers are in unit of 1/100 s. (g) A schematic illustration of NiSi growth within a Si nanowire. (h) A schematic illustration of growth of a NiSi/Si/NiSi heterostructure where the length of the Si section is controlled at the atomic scale [48].

based on Si nanowires are expected to have significant potential and wide interest. To realize this potential, nanoscale device elements such as ohmic contacts and gates on Si nanowires must be developed [49]. The formation of these device elements requires a systematic study of chemical reactions in the nanoscale. The point contact reactions between Si nanowires and Ni nanowires were investigated [47,48].

Ni and Si were selected for the study because the monosilicide NiSi is one of the three silicides which have the lowest resistivity for applications in shallow junction devices [50]. In addition, single crystal NiSi nanowires can be scaled to ultrasmall dimension without degradation of electrical conductivity and exhibit remarkably high maximum transport current [42]. Si nanowires were prepared on a Si wafer by the VLS method with nano-Au dots as nucleation sites for single-crystal Si nanowires with a [1 1 1] growth direction [51,52]. Polycrystalline Ni nanowires were synthesized via the anodic aluminum oxidation (AAO) method and stored in isoproponal [53]. The Ni nanowires and Si nanowires have diameters ranged from 10 nm to 40 nm and lengths of a few microns. The Si and Ni nanowires were stored in solutions. To prepare point contact samples, droplets of both solutions are put on Si grids having a square opening covered with a window of glassy Si_3N_4 films, as shown in Fig. 10(a). The thickness of the glassy film is about 20 nm so that it is transparent to the electron beam in the microscope and does not interfere with the images of Si and Ni nanowires. The samples were dried under light bulbs.

Fig. 10(b)–(f) shows a time-lapsed series of in situ TEM images capturing the growth of a bamboo-type NiSi grain within a straight Si nanowire at 700 °C. Based on the high-resolution TEM images and selected area diffraction patterns, we determined the structure of the material to be single-crystal NiSi. Fig. 10(g) is a schematic diagram depicting the growth of NiSi, in which the Ni atoms dissolve and diffuse interstitially in Si [54] and stop at the ends of the Si nanowire, thereby nucleating growth of NiSi to form a NiSi/Si/NiSi heterostructure. In point contact reaction, growth of single crystal NiSi started from both ends of the Si nanowire with an activation energy of 1.25 eV/atom rather than from the point contact with an activation energy of 1.7 eV/atom. This is attributed to the ease of nucleation and fast diffusion of Ni atoms in Si towards the ends.

Fig. 11 shows the linear growth behavior of the NiSi nanowire in the Si nanowire of 20 nm in diameter over the temperatures ranged from 500 °C to 650 °C. The activation energy of the epitaxial growth was determined to be 1.25 eV/atom, compared to the activation energy of interstitial diffusion of Ni in Si of about 0.47 eV/atom [55], indicating that the growth may be interfacial-reaction-controlled.

To identify the phase and structure of the NiSi nanowire, its HRTEM image is provided in Fig. 12(a). The inset is the corresponding diffraction pattern with a zone axis of [1 1 3], which verifies that the wire is a single crystal of NiSi. Compositional analysis has also confirmed that it is NiSi. Fig. 12(b) is a high-resolution TEM image showing an epitaxial interface which is atomically sharp between Si and NiSi within a Si nanowire. Fig. 12(a) and (b) demonstrates that point contact reaction enables the formation of nano-NiSi in perfect single crystal and atomically flat NiSi/Si interface without misfit dislocations, which is important for electrical contact properties.

The atomistic mechanism of the epitaxial growth involving a moving interface is of interest. Reactive epitaxial growth is unlike molecular beam epitaxy by deposition, in which atomic layers are built on the substrate surface and film growth requires no breaking of the substrate bonds. In the present case, the covalent Si–Si bonds must be broken and transformed into metallic Ni–Si bonds in order for NiSi to grow and have a moving interface.

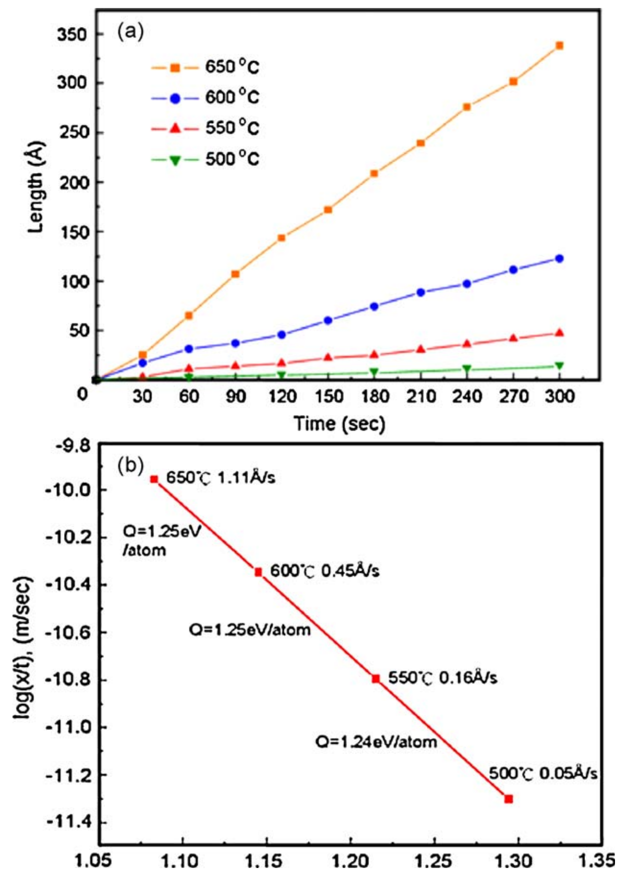

Fig. 11. Kinetic analysis of the NiSi epitaxial growth within a Si nanowire of 20 nm in diameter. (a) Plot of the NiSi nanowire length versus reaction time at various temperatures, illustrating a linear growth rate. The lines are drawn as guides. (b) Arrhenius plot of the NiSi epitaxial growth, from which the activation energy was determined [48].

Although the thermal energy at 700 °C is sufficient to break the covalent Si–Si bonds, the interstitial Ni atoms are crucial in the bond-breaking process [56].

Fig. 10(g) and (h) depicts the growth of NiSi from both ends of a Si nanowire. It leads to the formation of a NiSi/Si/NiSi nano-heterostructure as shown in Fig. 13(a) and (b). The darker regions at the two ends are NiSi and the lighter region in the middle is Si. If annealing is stopped before the entire nanowire transforms into NiSi, as in Fig. 13(c), a nano-heterostructure is formed as shown in Fig. 13(a) and (b). The nanoscale epitaxial growth rate of single-crystal NiSi has been measured using high resolution lattice imaging videos. Based on the growth rates, the remaining length of the Si region between the two NiSi regions can be controlled as illustrated in Fig. 10(h). Two Ni nanowires can be patterned or deposited with a given spacing over a Si wire, and then the reaction can be utilized to bring the two NiSi grains as close as possible. At 500 °C, the reaction rate can be controlled down to atomic scale. In Fig. 13(d)–(g), a set of lattice images of the nano-heterostructure of NiSi/Si/NiSi with 10, 8.1, 5 and 2 nm lengths of Si is shown. By measuring the length of the Si region and counting the number of (1 1 1) lattice planes within the region, the strain can be determined and it is found that the Si is highly compressed. Fig. 13(h) shows the relationship between the compressive strain and the length of the Si region in the nano-heterostructure NiSi/Si/NiSi at room temperature. In the process of NiSi formation, the diffusion of Ni atoms into Si lattice could have led to volume expansion. However, due to the confinement of the oxide on the Si nanowire, NiSi coming from both sides compressed the middle Si

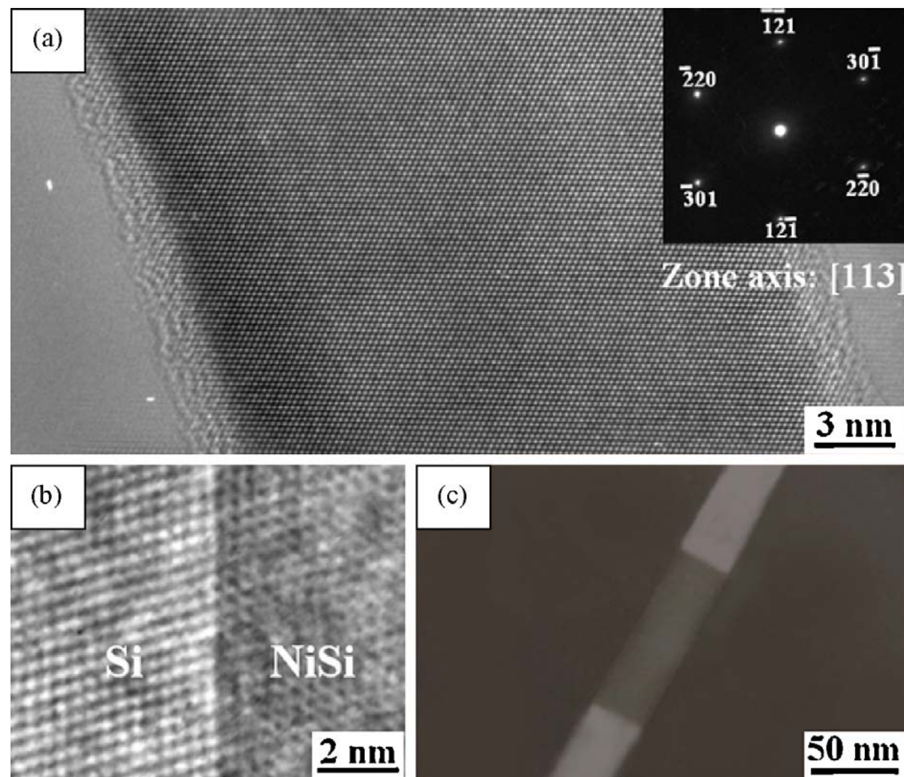

Fig. 12. (a) HRTEM image of a NiSi nanowire. The inset is the corresponding diffraction pattern with a [1 1 3] zone axis. (b) HRTEM image of an epitaxial interface between NiSi and Si within a Si nanowire. (c) High angle annular dark-field image of the NiSi/Si/NiSi heterostructure. The bright image is NiSi and the dark image is Si [47].

region, resulting in compressive stress on Si in the length direction. As a result, the strain increased when the length of the Si region decreased. The strain can be controlled because the length of the Si region can be controlled. Since one-dimensional nano-heterostructures may have potential applications in nanoelectronic devices [57], the strain will affect carrier mobility in the Si region.

To sum up, nano-heterostructures of NiSi/Si/NiSi, in which the length of the Si region can be controlled down to 2 nm, have been produced using in situ point contact reaction between Si and Ni nanowires in an UHV-TEM. The Si region was found to be highly strained, more than 12%. It is proposed that the reaction is assisted by interstitial diffusion of Ni atoms within the Si nanowire and is limited by the rate of dissolution of Ni into Si at the point contact interface. The rate of incorporation of Ni atoms to support the growth of NiSi has been measured to be 7×10^{-4} s per Ni atom. Based on the rate, the consumption of Si can be controlled and, in turn, the dimensions of the nano-heterostructure down to less than 2 nm, thereby far exceeding the limit of conventional patterning process. The controlled huge strain in the controlled atomic scale Si region, potential gate of Si-nanowire-based transistors, is expected to significantly impact the performance of electronic devices.

3.2. *Repeating events of nucleation in epitaxial growth of nano-$CoSi_2$ and NiSi in nanowires of Si [58,59]*

Nanostructures in Si nanowires have been studied for basic components in electronic and optoelectronics devices, especially biosensors [60–62]. Well-defined nanoscale building blocks such as ohmic contacts and gates on Si nanowires must be developed in order to be assembled into functional electronic structures [42,49,63]. It requires a systematic study of chemical reactions in the nanoscale to form these circuit components. When a Si nanowire touches a metal nanowire, a point contact is formed and the chemical reaction between them starts from the point of contact. The point contact reactions between Si nanowires and Ni and Co nanowires or nanodots were investigated by in situ HRTEM. The metallic NiSi and $CoSi_2$ may serve as the source-drain contacts to the Si in the heterostructure; it is the first step to produce a nanoscale field-effect transistor.

The formation of CoSi and $CoSi_2$ in Si nanowires was observed at 700 °C and 800 °C, respectively, by point contact reactions between nanodots of Co and nanowires of Si by in situ HRTEM. The $CoSi_2$ has undergone an axial epitaxial growth in the Si nanowire and a stepwise growth mode was found, as shown in Fig. 14(a)–(d). We observed that the stepwise growth occurs repeatedly in the form of an atomic step sweeping across the $CoSi_2$/Si interface, as shown in Fig. 14(e). It appears that the growth of a new step or a new silicide layer requires an independent event of nucleation. We are able to resolve the nucleation stage and the growth stage of each layer of the epitaxial growth in video images. In the nucleation stage, the incubation period is measured to be much longer than the period needed to grow the layer across the silicide/Si interface. So the epitaxial growth consists of a repeating nucleation and a rapid stepwise growth across the epitaxial interface. This is a general behavior of epitaxial growth in nanowires. The nucleation of silicides in Si nanowires is supply limited and source-limited reaction by point contact reaction rather than diffusion-controlled or interfacial controlled reaction. Besides, the axial heterostructure of $CoSi_2$/Si/$CoSi_2$ with sharp epitaxial interfaces has been obtained, which are promising as high performance transistors based on intrinsic Si nanowires.

The HRTEM videos show that the overall axial growth rate of the Ni and Co silicide layers is linear. However, the linear curve can be

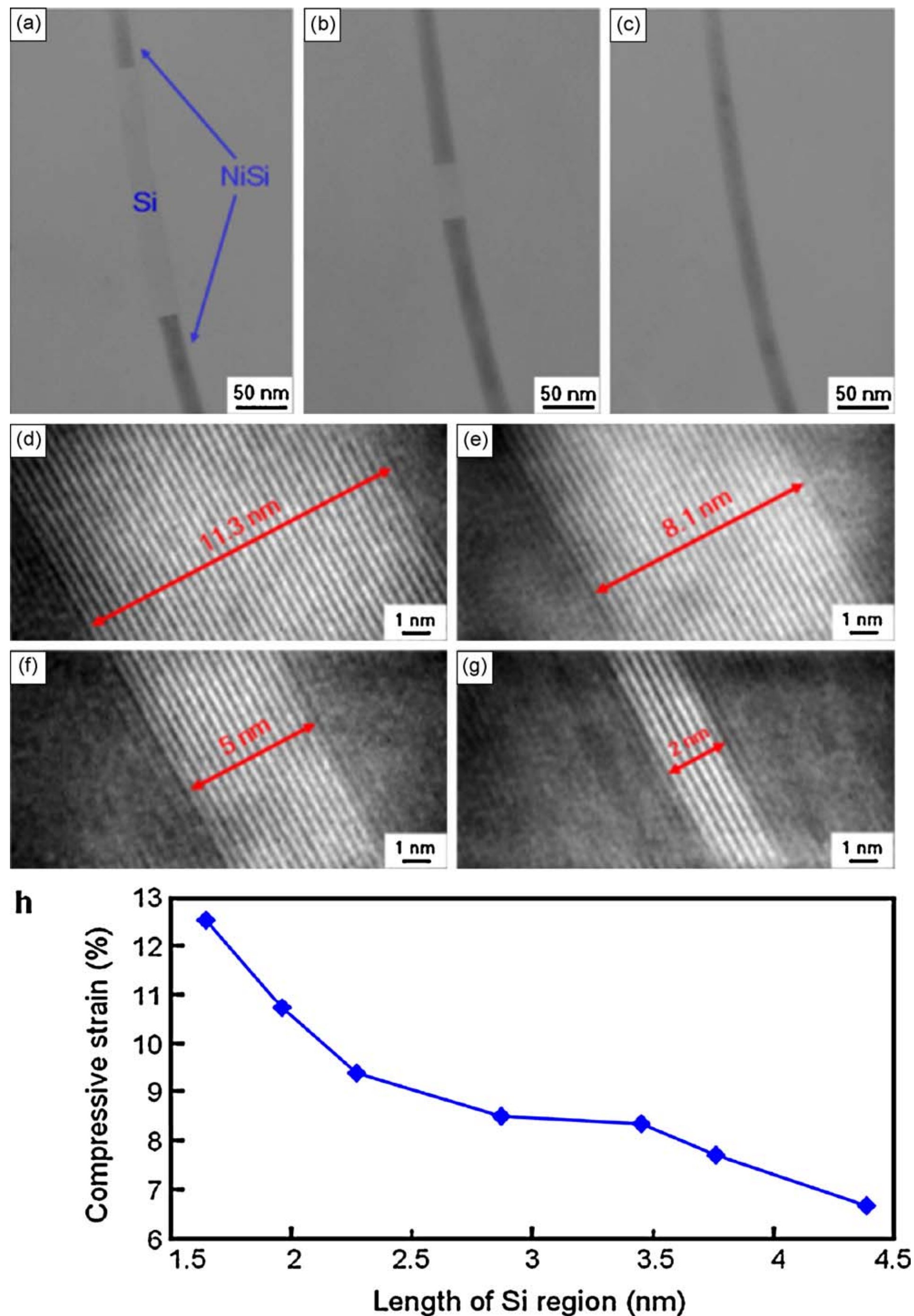

Fig. 13. In situ TEM images showing the formation of NiSi/Si/NiSi heterostructures within a Si nanowire, and compressive strain in the Si region. (a and b) In situ TEM images of the NiSi/Si/NiSi heterostructure. The bright area is Si and the dark area is NiSi. (d–g) HRTEM images of NiSi/Si/NiSi heterostructures. The bright and dark portions of the lattice images correspond to Si and NiSi, respectively. (h) Plot of the compressive strain versus the length of the Si region in the nano-heterostructure NiSi/Si/NiSi [48].

decomposed into many stair-steps with the step height equal to an atomic layer thickness and the step width equal to the incubation time of nucleating a new step. After a step is nucleated, it propagates very rapidly across the Si/silicide interface. The overall reaction rate is limited by the incubation time of nucleation, so it is a nucleation-limited reaction, neither diffusion-limited nor interfacial-reaction-limited.

Repeating events of homogeneous nucleation in epitaxial growth of $CoSi_2$ and NiSi silicides in Si nanowires by using in situ HRTEM was observed as shown in Fig. 15. The growth of every single atomic layer requires nucleation. Heterogeneous nucleation is prevented because of non-microreversibility between the oxide/Si and oxide/silicide interfaces so homogeneous nucleation occurs. The incubation time of homogeneous nucleation is determined to be 3 s and 6 s for NiSi and $CoSi_2$, respectively. Moreover, the calculated and the measured nucleation rates are in good agreement. Using Zeldovich factor to estimate the number of molecules in the critical nucleus; it is about 10 and reasonable. A very high supersaturation is found for the homogeneous nucleation.

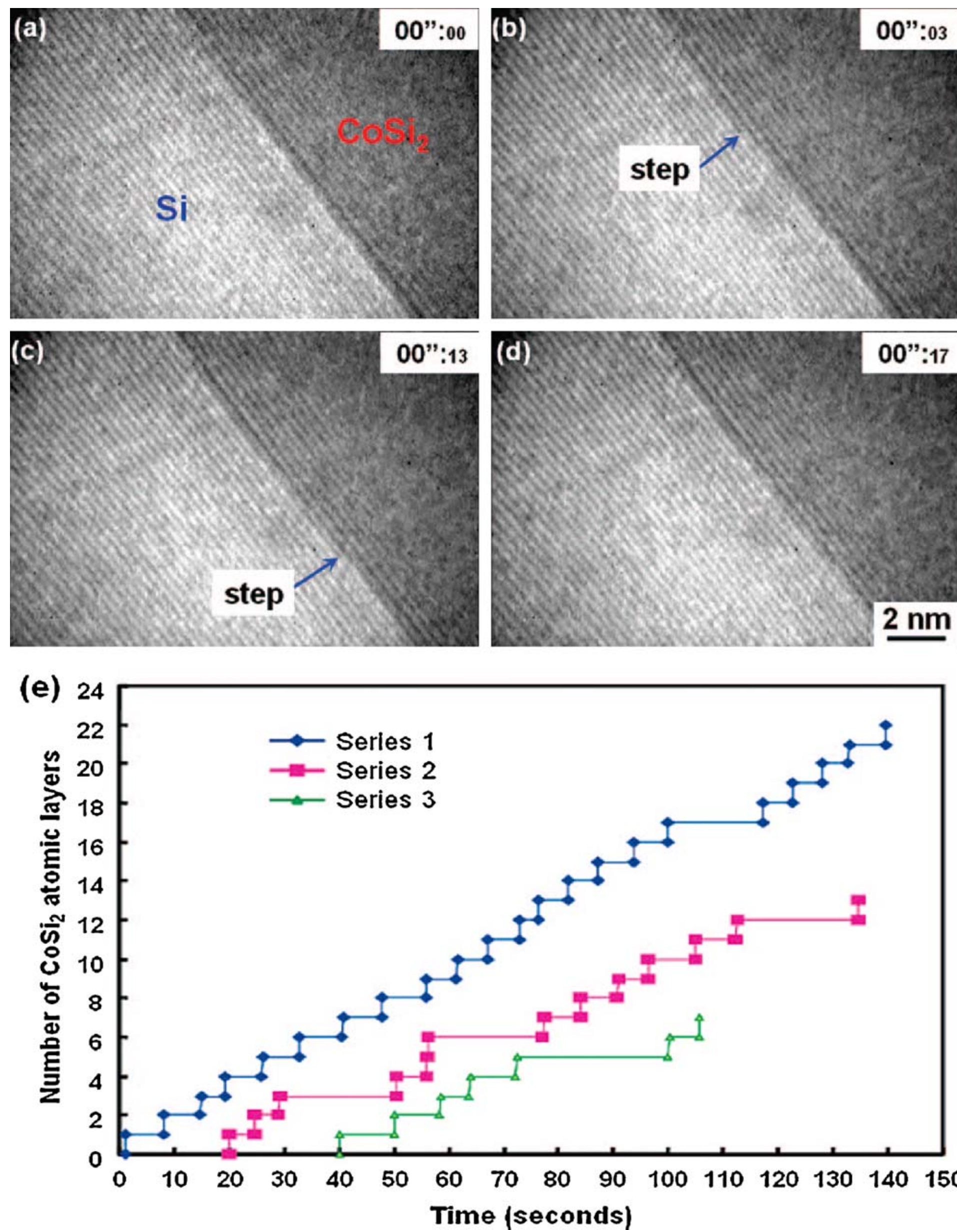

Fig. 14. In situ HRTEM image sequences of growing $CoSi_2$/Si epitaxial interfaces within Si nanowires. (a–d) the growth of one atomic layer has occurred, and the step is indicated by the arrow. The left-up and right-down regions are close to center and edge of nanowire, respectively. (e) Three sets of stair-type growth curve of $CoSi_2$ [58].

4. In situ TEM investigation of copper electromigration

4.1. In situ transmission electron microscope observations of electromigration in copper lines at room temperature [64,65]

With continuous miniaturization of integrated circuits (IC), the densities of electric current and heating power associated with the interconnecting wires in ICs are rising in a rather fast manner. Under a high current density of $\sim 10^6$ A/cm^2, some voids and hillocks may form in the interconnecting wires due to electromigration (EM) induced mass transport and eventually lead to device failures [66,67]. In advanced semiconductor process technology, copper has replaced aluminum as the interconnection material of choice due to its superior electrical conductivity and higher EM resistance. In recent years a number of in situ EM studies have been carried out by observing void and hillock formation on metal lines using scanning electron microscopy [68–70]. These measurements were usually done at elevated temperatures in order to observe EM-induced voiding or hillock formation within a reasonable time frame. In this study, in situ TEM observation of atomic-scale EM behavior in a Cu line is reported at room temperature. The effects of crystal orientation and anisotropic electric resistivity on atomic-scale Cu EM characteristics are also discussed.

Fig. 16 reveals the atomic images of Cu grain along [2 1 1] direction at different stages during electric current stressing. It is noted that the direction of electron flux is from the right to the left of the micrographs. Interestingly, the Cu atomic images appeared to fade gradually from the lower-left of the examined grain. Moreover, the atomic images of the grain disappeared completely after stressing the Cu line for 25 min. It is a strong indication of EM-induced atomic movement in the Cu grain. By examining the sequential HRTEM images carefully, the atomic images of Cu grain did not seem to shrink equally in all directions. Instead, the (2 1 1) lattice image faded away from the edge of the $(1\,\bar{1}\,\bar{1})$ lattice plane along the $[0\,1\,\bar{1}]$ direction. It is noted that Cu surface diffusion on

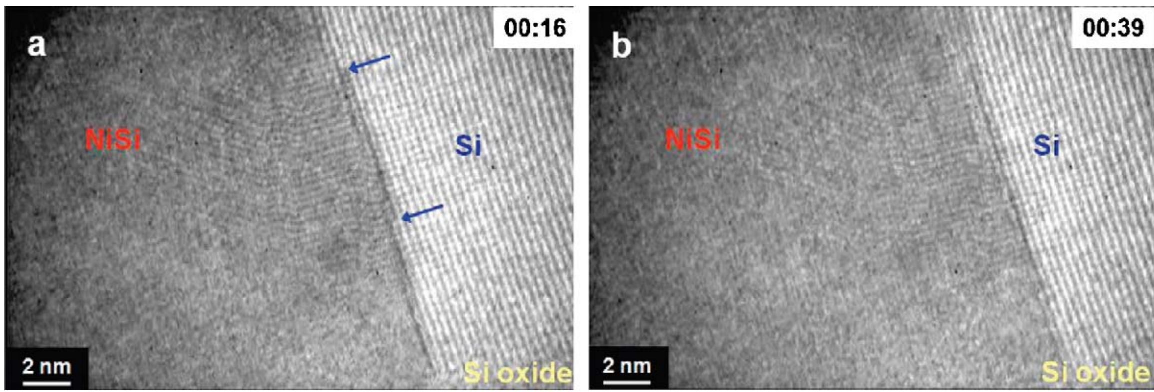

Fig. 15. HRTEM images of motion of steps on epitaxial NiSi/Si interface at 450 °C. (a) One NiSi atomic layer grows from the middle region of the interface. (b) After two steps reaches to the oxide ends, the layer growth ends and the interface becomes flat without steps [59].

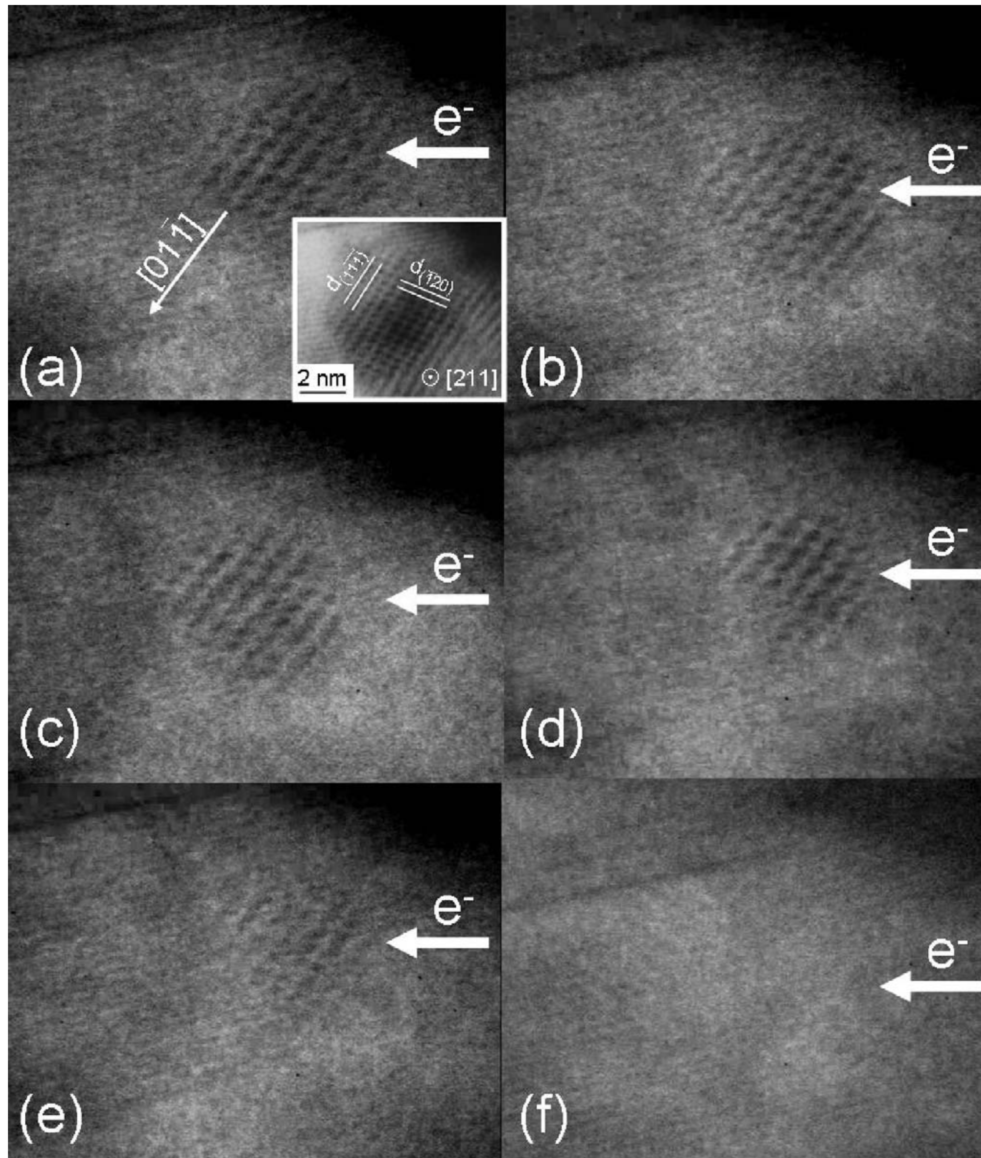

Fig. 16. Real-time HRTEM images of a thin Cu line under electric current stressing recorded at (a) 6 min (b) 9 min (c) 12 min (d) 15 min (e) 21 min (f) 25 min. The inset is HRTEM image of the (2 1 1) grain with two intersecting lattice planes.

different crystal planes has distinct migration energies. Face-center-cubic crystal structure, in general, has the lowest migration energy on {1 1 1} planes among the major low-index planes [71,72]. It was reported that the partial resistivities of Cu in the directions of [1 0 0], [1 1 0] and [1 1 1] at room temperature and found them in the order of $\rho_{[111]} > \rho_{[100]} > \rho_{[110]}$ [73]. It implies that electrons flowing in the ⟨1 1 0⟩ directions would experience less resistance than in the ⟨1 1 1⟩ directions. By applying a voltage across a crystalline copper, the partial current density in the ⟨1 1 0⟩ directions is expected to be higher than that in the ⟨1 1 1⟩ directions. Based on the anisotropic diffusion and electrical resistivity of crystalline copper, the combination of {1 1 1} planes and ⟨1 1 0⟩ directions is suggested to be the most favorable electromigration system inside a grain, which is well supported by in situ TEM observations of atomic-scale Cu EM behavior.

Fig. 17 shows the HRTEM images of Cu atoms on $(0\,1\,\bar{1})$ crystal planes in the stressed Cu line as a function of time. The atomic images clearly show two intersecting lattice planes, (1 1 1) and $(1\,\bar{1}\,\bar{1})$, with a zone axis in the $[0\,1\,\bar{1}]$ direction. The atomic images were found to disappear gradually from right to the left in the same direction as the electron flow. Interestingly, a surface step structure has been observed at the side wall of the atomic image shown in Fig. 17(b), which is consistent with the proposed EM system when the dominant surface diffusion mechanism is assumed. These findings lead to the conclusion that Cu (1 1 1) oriented grains are more susceptible to EM damage than others when surface diffusion is a dominant migration mechanism. Moreover, the observed EM-induced surface step structure also provides a clue of interfacial voiding in Cu interconnections. Although a variety of techniques have been proposed to inhibit the EM-induced interconnect voiding, including plasma treatment of Cu metallization, dielectric passivation and metal capping [74–76], the results sometimes are inconclusive. It is because the EM-induced failure mechanism depends on crystal orientation and surface structure of Cu interconnections, which can be easily modified by thin film deposition, etching and thermal treatment processes in IC fabrication. With the in situ TEM technique we are capable of directly observing the EM paths of Cu atoms on a single grain with different crystal orientations, which would lead to the effective strategy for passivation to suppress the electromigration.

4.2. Observation of atomic diffusion at twin-modified grain boundaries in copper [77]

Grain boundaries affect the migration of atoms and electron in polycrystalline solids, thus influencing many of the mechanical and electrical properties [78]. By introducing nanometer-scale twin defects into copper grains, we show that we can change the grain-boundary structure and atomic-diffusion behavior along the boundary. Using in situ HRTEM, we observed electromigration-induced atomic diffusion in the twin-modified grain boundaries. The triple point where a twin boundary meets a grain boundary was found to slow down grain-boundary and surface electromigration by one order of magnitude. Fig. 18 shows a set of HRTEM images of a twin-modified grain boundary at different stages during electric current stressing. The grain has several {1 1 1}/⟨1 1 2⟩-type coherent twin boundaries. Under the influence of EM, the edge of this (0 1 1)-oriented grain in the grain-boundary plane has evolved into a zigzag shape [79]. We observed that an atomic step appeared at the triple point of the twin boundary (TB1) in Fig. 18 and moved rather rapidly on the $(1\,\bar{1}\,\bar{1})$ plane toward the other triple point of the twin boundary (TB2). The results indicate that the Cu atoms move on the $(1\,\bar{1}\,\bar{1})$ surface along the direction of electron flux, resulting in the atomic step moving in the opposite direction. Once the atomic step reached TB2, we observed that it was trapped for a while before moving out onto $(4\,\bar{2}\,\bar{2})$ plane. By tracing the atomic steps moving along the $(1\,\bar{1}\,\bar{1})$ and $(4\,\bar{2}\,\bar{2})$ planes, we can plot the distances of different atomic steps from TB1 and TB2, with respect to time, as shown in the Fig. 19. We found that there exists a time lag of ~5 s for the atomic steps to cross the triple points under electric current stressing. The moving speed of the atomic step on the $(1\,\bar{1}\,\bar{1})$ and $(4\,\bar{2}\,\bar{2})$ surfaces were calculated to be 5.7 nm/s and 3.4 nm/s, respectively. Because of the {1 1 1} planes have the lowest atomic-migration energies among the major low-index planes of Cu. Nevertheless, the most important finding is that the triple point can slow down or block the EM-induced atomic migration in the twin-modified grain boundaries of Cu.

It is remarkable that the sample had more than one free surface; thus, atoms diffused along more than one direction or plane. The plane perpendicular to the electron beam was also a free surface

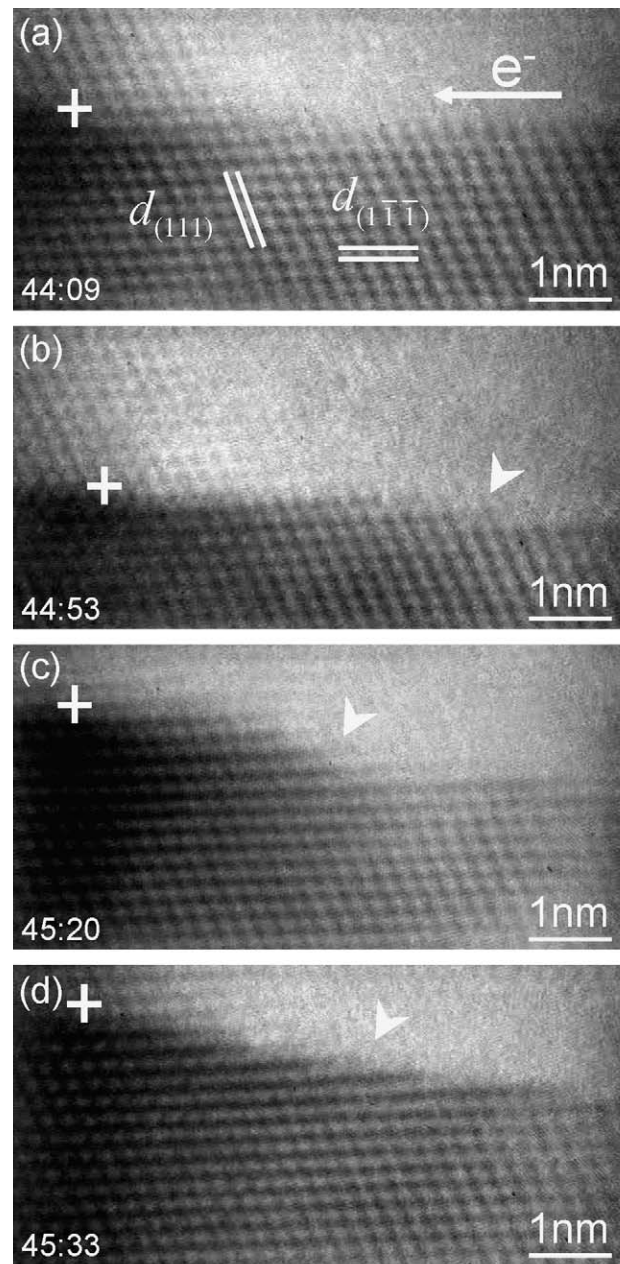

Fig. 17. The HRTEM images of Cu atoms on the $(0\,1\,\bar{1})$ crystal planes in the stressed Cu line as a function of time. The HRTEM images were analyzed by fast Fourier transform (FFT) techniques. The arrows labeled indicate the atomic surface steps on the Cu $(1\,\bar{1}\,\bar{1})$ crystal planes. The cross referred to a fixed point for the ease of inspection [64].

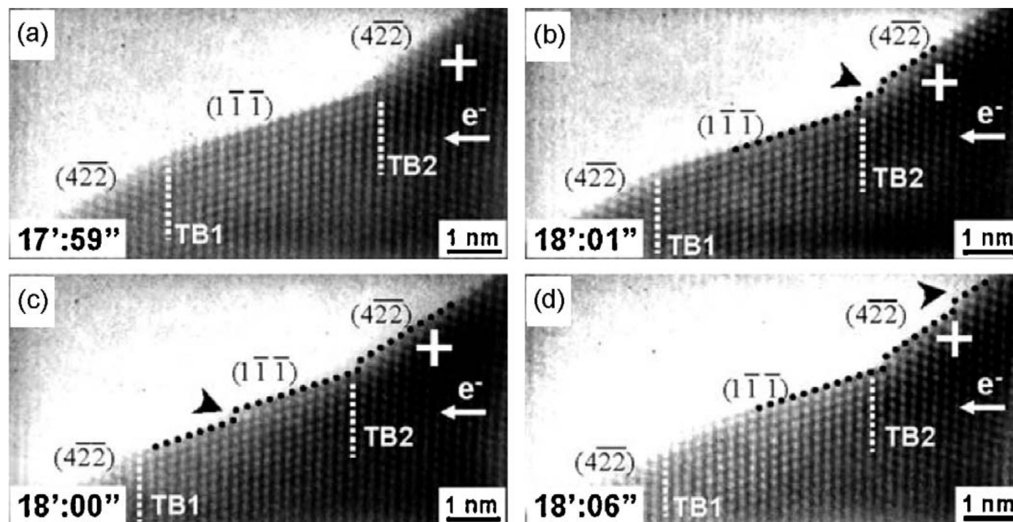

Fig. 18. (a–d) HRTEM images of the (0 1 $\bar{1}$) -oriented Cu grain under electric current stressing as a function of time. The time of the image capture (in minutes and seconds) is given in the rectangular box at the lower left corner. The direction of electron flow is from right to left. The arrowheads indicate the atomic steps on the lattice planes. The cross in each panel refers to a fixed point for ease of inspection. The HRTEM image was analyzed by fast Fourier transform technique [65].

along which atoms diffused during the process. Due to the migration of the plane, the thickness decreased and atomic columns disappeared eventually as observed in our experiment. Furthermore, the effect of electron beam damage was also minimal in this work.

5. Growth kinetics of semiconducting nanowires [3,80]

Due to applications in nanotechnology, silicon nanowires have been drawing increasing attention and interest, especially promising in nanoelectronics for the capability of engineering nanowire properties. The most common way of growing Si nanowires is the vapor–liquid–solid method. Despite being studied for over 40 years, certain aspects of VLS mechanism remain unclear. For example, it is conventionally assumed that no change occurs in the catalyst droplet during growth and that the nanowire sidewalls are composed of clean silicon facets. However, Hannon et al. demonstrated that the above assumptions are not true for silicon nanowires grown on Si(1 1 1) under carefully controlled experimental parameters, including surface structure, gas cleanliness, and background contaminants. They showed that it is the gold diffusion during growth that controls the length, shape, and sidewall properties of the nanowires. Wetting the nanowire sidewalls, gold from the catalyst droplets eventually consumes the droplets and terminates VLS growth. Gold diffuses from the smaller droplets to the larger ones, a phenomenon of Ostwald ripening, contributing to change of nanowire diameters during growth [3]. These results suggest that the silicon nanowire growth be fundamentally limited by gold diffusion; in other words, growth of arbitrarily long and smooth nanowires requires elimination of gold migration.

On the other hand, it has been observed that nanowires grow below the eutectic temperature, and the state of the catalyst has been uncertain. Utilizing in situ TEM, Kodambaka et al. reported that, for the classic Ge/Au system, nanowire growth can happen below the eutectic temperature with either liquid or solid catalysts at the same temperature [80]. Another finding is that the catalyst state is unexpectedly determined by the growth pressure and thermal history. They indicated that kinetic enrichment of the eutectic alloy composition may result in these phenomena, expected to be relevant for other nanowire systems.

6. Nanothermometry

In the development of nanotechnology, high sensitivity temperature sensor is urgently needed for both fundamental understanding of nanosystems and functional applications. Fabrication of nanothermometer based on core/shell nanostructures has recently attracted enormous attention. The operations of those nanothermometers were based on calibrating temperature with thermal expansion of filled metals in the TEM [81]. Recently, Gong et al. reported a reversible wide range high temperature nanothermometer (10 nm/100 K with 670 nm Au(Si) filling in Ga_2O_3 with a high CTE ($150 \times 10^{-6}\,K^{-1}$) at temperatures higher than 300 °C [82]. All these nanothermometers work with the filling materials in liquid-like or liquid state. Yet, it is still a tremendous challenge to fabricate high sensitivity nanothermometer working in solid state at a temperature range of room temperature to about 300 °C. The primary advantage of a solid state nanothermometers is that the demand on the structural integrity is considerably less for the outer shell. Unlike liquid filling materials, solid is not prone to leak out.

Among all the elements, solid lead (Pb) exhibits the highest thermal expansion with the exception of mercury (Hg) and alkali metals at room temperature. Bulk Pb has a linear CTE of $30 \times 10^{-6}\,K^{-1}$ (linear 0–300 °C) and the CTE of Hg is $60 \times 10^{-6}\,K^{-1}$. However, mercury is in liquid state and alkali metals are hazardous at room temperature. Changes in the dimension in the ZnO nanotubes can be disregarded since the thermal expansion of the ZnO is rather small ($4 \times 10^{-6}\,K^{-1}$). As a result, solid Pb is potentially useful as the filling material in nanothermometers.

Galvanic displacement method was used to fabricate Pb(core)/ZnO(shell) nanostructures and their application as high sensitivity nanothermometer. The Pb/ZnO nanocables were spontaneously reduced to nanostructures grown on zinc substrate at room temperature [83]. The thermal expansion of Pb/ZnO nanocables is readily detected at low temperature since the lengths of nanocables and could be grown to a few tens of micrometers and the inner Pb fillings are sufficiently long. The Pb–ZnO system is unique in that it is the only available nanothermometer operating in solid state. Compare to liquid thermal expansion, solid state nanothermometer is advantageous for much less demanding on

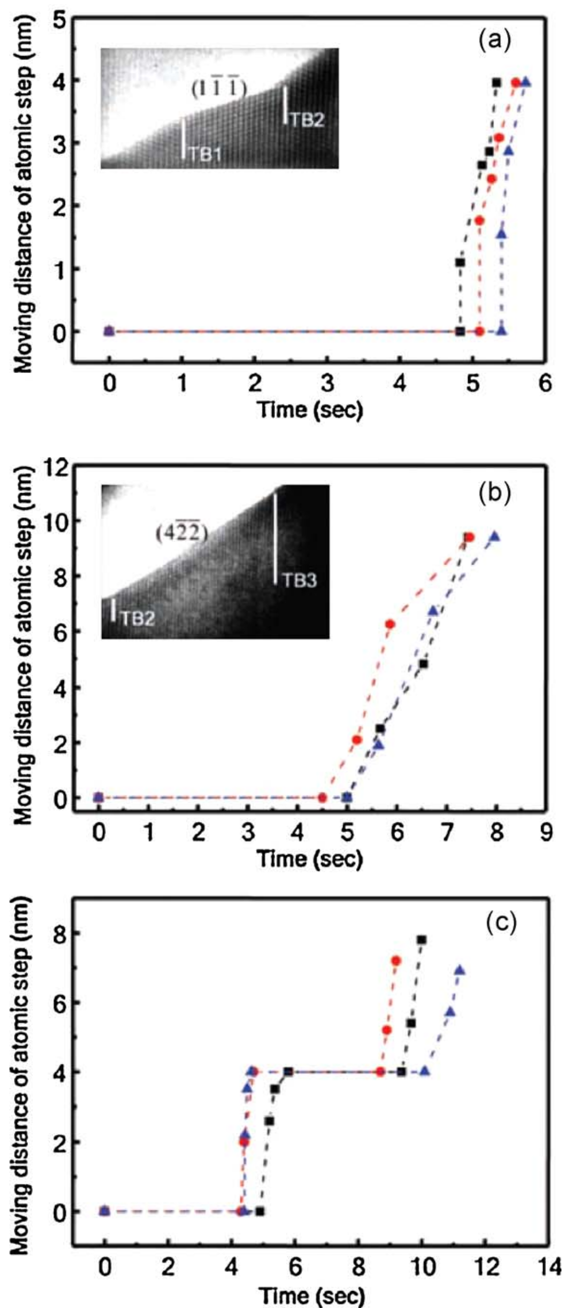

Fig. 19. Movement of different atomic steps on (a) the (1 1̄ 1̄) surface, (b) the (4 2̄ 2̄) surface, and (c) the surface between TB1 and TB3 as a function of time. Insets in (a) and (b) show the moving trace of the atomic steps. Black squares, atomic step 1; red circles, atomic step 2; blue triangles, atomic step 3 [77]. (For interpretation of the references to color in this figure legend, the reader is referred to the web version of the article.)

the structural integrity of the outer shell and with superior reliability [84].

7. Conclusions

In situ TEM has provided a very useful method to directly measure the dynamic changes of nanostructures on Si. Through observing growth and phase transitions in situ, we can understand their mechanisms and model relevant processes. With the precise knowledge of the changes occurring in atomic scale, accurate control of the growth process can be achieved. In situ TEM will definitely continue to contribute to the major advance in the nanoscience and nanotechnology in the future.

Acknowledgments

The work was supported by the National Science Council through grant nos. 97-2120-M-007-003 and 96-2628-E-007-018-MY3. The authors would like to acknowledge the contributions from Profs. K.N. Tu, C.N. Liao, J.H. He and K.C. Lu.

References

[1] Y. Cui, C.M. Lieber, Science 291 (2001) 851.
[2] Y. Xia, P. Yang, Y. Sun, Y. Wu, B. Mayers, B. Gates, Y. Yin, F. Kim, H. Yan, Adv. Mater. 15 (2003) 353.
[3] J.B. Hannon, S. Kodambaka, F.M. Ross, R.M. Tromp, Nature 440 (2006) 69.
[4] J.H. He, W.W. Wu, S.W. Lee, L.J. Chen, Y.L. Chueh, L.J. Chou, Appl. Phys. Lett. 86 (2005) 263109.
[5] P.Y. Su, M.Y. Lu, J.C. Hu, S.L. Cheng, L.J. Chen, J.M. Liang, Appl. Phys. Lett. 87 (2005) 163101.
[6] P.Y. Su, J.C. Hu, S.L. Cheng, L.J. Chen, J.M. Liang, Appl. Phys. Lett. 84 (2004) 3480.
[7] Z.L. Wang, Adv. Mater. 15 (2003) 1497.
[8] H. Poppa, J. Vac. Sci. Technol. A22 (2004) 1931.
[9] J.H. He, W.W. Wu, Y.L. Chueh, C.L. Hsin, L.J. Chen, L.J. Chou, Appl. Phys. Lett. 87 (2005) 223102.
[10] R.J. Warburton, C. Schulhauser, D. Haft, C. Schaflein, K. Karrai, J.H. Garcia, W. Schoenfeld, P.M. Petroff, Phys. Rev. B 65 (2002) 113303.
[11] H. Pettersson, R.J. Warburton, A. Lorke, K. Karrai, J.P. Kotthaus, J.M. Garcia, P.M. Petroff, Physica E 6 (2000) 510.
[12] J.M. Garcia, T.M. Mankad, P.O. Holtz, P.J. Wellman, P.M. Petroff, Appl. Phys. Lett. 72 (2001) 1857.
[13] R.J. Warburton, C. Schaflein, D. Haft, F. Bickel, A. Lorke, K. Karrai, J.M. Garcia, W. Schoenfeld, P.M. Petroff, Nature 405 (2000) 926.
[14] T. Raz, D. Ritter, G. Bahir, Appl. Phys. Lett. 82 (2003) 1706.
[15] J.M. Garcia, G. Medeiros-Ribeiro, K. Schmidt, T. Ngo, J.L. Feng, A. Lorke, J. Kotthaus, P.M. Petroff, Appl. Phys. Lett. 71 (1997) 2014.
[16] J.H. He, Y.L. Chueh, W.W. Wu, S.W. Lee, L.J. Chen, L.J. Chou, Thin Solid Films 469 (2004) 478.
[17] K.L. Hobbs, P.R. Larson, G.D. Lian, J.C. Keay, M.B. Johnson, Nano Lett. 4 (2004) 167.
[18] D.R. Gaskell, Introduction to the Thermodynamics of Materials, 4th ed., Taylor & Francis, Washington, DC, 2003.
[19] C.H. Liu, W.W. Wu, L.J. Chen, Appl. Phys. Lett. 88 (2006) 023117.
[20] H.J. Fan, W. Lee, R. Scholz, A. Dadgar, A. Krost, K. Nielsch, M. Zacharias, Nanotechnology 16 (2005) 913.
[21] J.H. He, C.S. Lao, L.J. Chen, D. Davidovic, Z.L. Wang, J. Am. Chem. Soc. 127 (2005) 16376.
[22] J. Carrey, J.L. Maurice, P. Jensen, A. Vaures, Appl. Surf. Sci. 164 (2000) 48.
[23] A.A. Schmidt, H. Eggers, K. Herwig, R. Anton, Surf. Sci 349 (1996) 301.
[24] P. Deltour, J.L. Barrat, P. Jensen, Phys. Rev. Lett. 78 (1997) 4597.
[25] S.C. Wang, G. Ehrlich, Phys. Rev. Lett. 79 (1997) 4234.
[26] R.C. Jaklevic, L. Elie, Phys. Rev. Lett. 60 (1988) 120.
[27] D.W. Pashley, M.H. Jacobs, M.J. Stowell, T.J. Law, Philos. Mag. 10 (1964) 127.
[28] Q.Y. Tong, U. Göesele, Semiconductor Wafer Bonding, Electrochem. Soc., Pennington, NJ, 1998.
[29] J.L. Gardea-Torresdey, J.G. Parsons, E. Gomez, J. Peralta-Videa, H.E. Troiani, P. Santiago, M.J. Yacaman, Nano Lett. 2 (2002) 397.
[30] F. Liu, Phys. Rev. Lett. 89 (2002) 246105.
[31] S. Iijima, T. Ichihashi, Phys. Rev. Lett. 56 (1986) 616.
[32] A. Bourret, Surf. Sci. 432 (1999) 37.
[33] C.H. Liu, W.W. Wu, L.J. Chen, Appl. Phys. Lett. 88 (2006) 133112.
[34] W.C. Yang, H. Ade, R.J. Nemanich, Phys. Rev. B 69 (2004) 045421.
[35] B. Bokhonov, M. Korchagin, J. Alloy Compd. 312 (2000) 238.
[36] Y. Wakayama, H. Fujinuma, S. Tanaka, Mater. Res. 13 (1998) 1492.
[37] H.C. Hsu, W.W. Wu, H.F. Hsu, L.J. Chen, Nano Lett. 7 (2007) 885.
[38] X.Y. Kong, Z.L. Wang, Nano Lett. 3 (2003) 1625.
[39] J.Q. Hu, Y. Bando, Z.W. Liu, T. Sekiguchi, D. Golberg, J.H. Zhan, J. Am. Chem. Soc. 125 (2003) 11306.
[40] E.A. Stach, P.J. Pauzauskie, T. Kuykendall, J. Goldberger, R.R. He, P.D. Yang, Nano Lett. 3 (2003) 867.
[41] Y.L. Chueh, M.T. Ko, L.J. Chou, L.J. Chen, C.S. Wu, C.D. Chen, Nano Lett. 6 (2006) 1637.
[42] Y. Wu, J. Xiang, C. Yang, W. Lu, C.M. Lieber, Nature 430 (2004) 61.
[43] Z. He, D.J. Smith, P.A. Bennett, Phys. Rev. Lett. 93 (2004) 256102.
[44] Y. Chen, D.A.A. Ohlberg, G. Medeiros-Ribeiro, Y.A. Chang, Appl. Phys. Lett. 76 (2000) 4004.
[45] A.L. Schmitt, M.J. Bierman, D. Schmeisser, F.J. Himpsel, S. Jin, Nano Lett. 6 (2006) 1617.
[46] K.N. Tu, J.W. Mayer, L.C. Feldman, Electronic Thin Film Science, Macmillian Publishing, New York, 1992.
[47] K.C. Lu, K.N. Tu, W.W. Wu, L.J. Chen, B.Y. Yoo, N.V. Myung, Appl. Phys. Lett. 90 (2007) 253111.
[48] K.C. Lu, W.W. Wu, H.W. Wu, C.M. Tanner, J.P. Chang, L.J. Chen, K.N. Tu, Nano Lett. 7 (2007) 2389.

[49] L.J. Chen, JOM 57 (9) (2005) 24.
[50] F. Nava, K.N. Tu, O. Bisi, Mater. Sci. Rep. 9 (1993) 141.
[51] R.S. Wagner, W.C. Ellis, Appl. Phys. Lett. 4 (1964) 89.
[52] A.M. Morales, C.M. Lieber, Science 279 (1998) 208.
[53] S. Shingubara, O. Okino, Y. Sayama, H. Sakaue, T. Takahagi, Solid State Electron. 43 (1999) 1143.
[54] F.H.M. Spit, D. Gupta, K.N. Tu, Phys. Rev. B 39 (1989) 1255.
[55] E.R. Weber, Appl. Phys. A 30 (1983) 1.
[56] K.N. Tu, Appl. Phys. Lett. 27 (1975) 221.
[57] W.M. Weber, L. Geelhaar, A.P. Graham, E. Unger, G.S. Duesberg, M. Liebau, W. Pamler, C. Cheze, H. Riechert, P. Lugli, F. Kreupl, Nano Lett. 6 (2006) 2660.
[58] Y.C. Chou, W.W. Wu, S.L. Cheng, B.Y. Yoo, N. Myung, L.J. Chen, K.N. Tu, Nano Lett. 8 (2008) 2194.
[59] Y.C. Chou, W.W. Wu, L.J. Chen, K.N. Tu, Nano Lett. 9 (2009) 2337.
[60] L.J. Chen, J. Mater. Chem. 17 (2007) 4639.
[61] V. Schmidt, H. Riel, S. Senz, S. Karg, W. Riess, U. Gösele, Small 2 (2006) 85.
[62] F. Patolsky, B.P. Timko, G. Zheng, C.M. Lieber, MRS Bull. 32 (2007) 142.
[63] Y.C. Lin, K.C. Lu, W.W. Wu, J. Bai, L.J. Chen, K.N. Tu, Y. Huang, Nano Lett. 8 (2008) 913.
[64] C.N. Liao, K.C. Chen, W.W. Wu, L.J. Chen, Appl. Phys. Lett. 87 (2007) 141903.
[65] K.C. Chen, C.N. Liao, W.W. Wu, L.J. Chen, Appl. Phys. Lett. 90 (2007) 203101.
[66] C.L. Arnaud, T. Berger, G. Reimbold, J. Appl. Phys. 93 (2003) 192.
[67] E. Liniger, C.K. Hu, L. Gignac, A. Simon, J. Appl. Phys. 93 (2003) 9576.
[68] K.L. Lee, C.K. Hu, K.N. Tu, J. Appl. Phys. 78 (1995) 4428.
[69] E. liniger, L. Gignac, C.K. Hu, S. Kaldor, J. Appl. Phys. 92 (2002) 1803.
[70] T.G. Koetter, H. Wendrock, H. Schuehrer, C. Wenzel, K. Wetzig, Microelectron. Reliab. 40 (2000) 1295.
[71] C.L. Liu, J.M. Cohen, J.B. Adams, A.F. Voter, Surf. Sci. 253 (1991) 334.
[72] M. Karimi, T. Tomkowski, Phys. Rev. B 52 (1995) 5364.
[73] A. Magnaterra, Phys. Lett. 44A (1973) 63.
[74] A.V. Vairagar, S.G. Mhaisalkar, A. Krishnamoorthy, Thin Solid Films 462 (2004) 325.
[75] C.K. Hu, L. Gignac, R. Rosenberg, E. Liniger, J. Rubino, C. Sambucetti, A. Domenicucci, X. Chen, A.K. Stamper, Appl. Phys. Lett. 81 (2002) 1782.
[76] C.K. Hu, L. Gignac, E. Liniger, B. Herbst, D.L. Rath, S.T. Chen, S. Kaldor, A. Simon, W.-T. Tseng, Appl. Phys. Lett. 83 (2003) 869.
[77] K.C. Chen, W.W. Wu, C.N. Liao, L.J. Chen, K.N. Tu, Science 321 (2008) 1066.
[78] L. Lu, Y. Shen, X. Chen, L. Qian, K. Lu, Science 304 (2004) 422.
[79] L.D. Marks, D.J. Smith, Nature 303 (1983) 316.
[80] S. Kodambaka, J. Tersoff, M.C. Reuter, F.M. Ross, Science 316 (2007) 729.
[81] Y. Gao, Y. Bando, Nature 415 (2002) 599.
[82] N.W. Gong, M.Y. Lu, C.Y. Wang, Y. Chen, L.J. Chen, Appl. Phys. Lett. 92 (2008) 073101.
[83] C.Y. Wang, M.Y. Lu, H.C. Chen, L.J. Chen, J. Phys. Chem. C 111 (2007) 6215.
[84] C.Y. Wang, N.W. Gong, L.J. Chen, Adv. Mater. 20 (2008) 4789.